CHALMERS
UNIVERSITY OF TECHNOLOGY

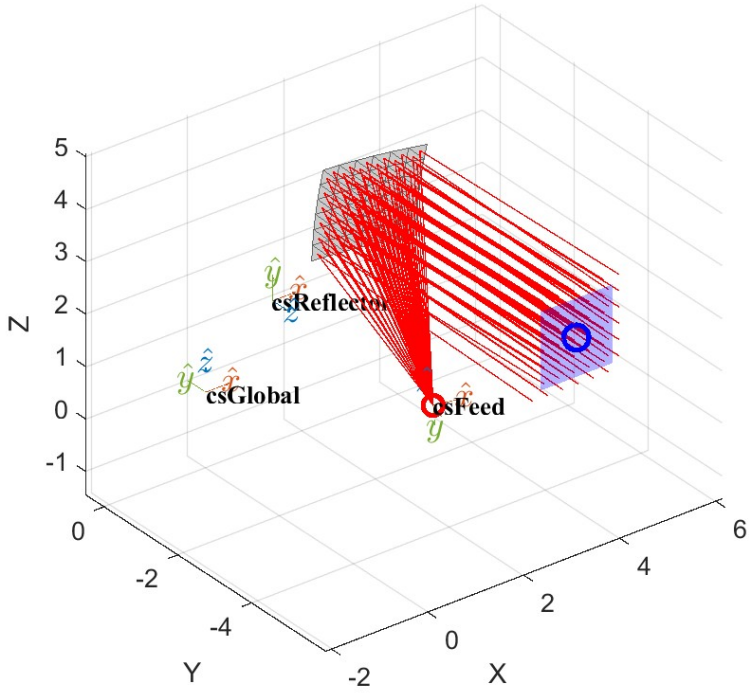

Electromagnetic Simulation of a CATR for Digital Twin Development

An Investigation of Virtual OTA Chamber Development for Quiet Zone Analysis Using Electromagnetic Solvers

Master's thesis in Information & Communication Technology

Christoffer Lennernäs
Rasmus Gyllenhammar

DEPARTMENT OF ELECTRICAL ENGINEERING
CHALMERS UNIVERSITY OF TECHNOLOGY
Gothenburg, Sweden 2026
www.chalmers.se

Master's thesis 2026

Electromagnetic Simulation of a CATR for Digital Twin Development

An Investigation of Virtual OTA Chamber Development for Quiet Zone Analysis Using Electromagnetic Solvers

Christoffer Lennernäs
Rasmus Gyllenhammar

CHALMERS
UNIVERSITY OF TECHNOLOGY

DEPARTMENT OF ELECTRICAL ENGINEERING
Division of Communications, Antennas, and Optical Networks
Chalmers University of Technology
Gothenburg, Sweden 2026

Electromagnetic Simulation of a CATR for Digital Twin Development
An Investigation of Virtual OTA Chamber Development for Quiet Zone Analysis Using Electromagnetic Solvers
Christoffer Lennernäs
Rasmus Gyllenhammar

Supervisor: Anders Jernberg, Ericsson Company
Supervisor: Oleg Iupikov, Department of Electrical Engineering
Examiner: Rob Maaskant, Department of Electrical Engineering

Master's Thesis 2026
Department of Electrical Engineering
Chalmers University of Technology
SE-412 96 Gothenburg
Telephone +46 31 772 1000

Cover: The feed, reflector and Quiet Zone plane in the CATR model. Printed by Chalmers Reproservice
Gothenburg, Sweden 2026

Electromagnetic Simulation of a CATR for Digital Twin Development
An Investigation of Virtual OTA Chamber Development for Quiet Zone Analysis Using Electromagnetic Solvers

Christoffer Lennernäs
Rasmus Gyllenhammar

Department of Electrical Engineering
Chalmers University of Technology

Abstract

This thesis presents the development of a simulation model of an Over-The-Air (OTA) Compact Antenna Test Range (CATR) chamber as an initial step toward a digital twin of Ericsson's OTA environment. The work investigates how scattering objects and different chamber configurations affect Quiet Zone (QZ) performance. Electromagnetic simulations were performed using Physical Optics (PO) and Method of Moments (MoM) formulations to evaluate field distributions and to study QZ characteristics such as amplitude, phase, and ripple variations.

The results show that the model can reproduce some qualitative features of OTA chamber behavior, particularly QZ degradation due to scattering objects and reflector geometry. Comparison between PO and MoM highlights limitations of the PO approximation, especially where edge effects dominate, leading to discrepancies in field distribution and ripple behavior near reflector edges.

Despite these limitations, the model enables useful comparative analysis of chamber configurations. Variations in reflector geometry and the presence of scattering objects consistently affect QZ uniformity, influencing both amplitude and phase distributions. The study also indicates that improvements from serrated reflector edges are mainly linked to an increased effective reflecting area.

Overall, the simulation framework provides a first modelling step toward a future digital twin of the OTA chamber. While absolute accuracy is limited by the current electromagnetic formulation, the model is useful for studying relative QZ degradation and guiding future improvements in chamber design and simulation fidelity.

Keywords: CATR, Anechoic Chamber, Physical Optics, Method of Moments, Quiet Zone, Digital Twin, Ericsson.

Acknowledgements

We would like to express our sincere gratitude to Oleg and Rob for their invaluable support throughout this project. Their guidance in algorithm development, assistance with coding and debugging, and deep expertise in electromagnetics were essential to the completion of this thesis. The many insightful discussions and their continuous willingness to share knowledge greatly contributed to both the direction and quality of our work.

We would also like to thank Jean-Marc Pierre and Anders Jernberg from Ericsson for giving us the opportunity to carry out our master's thesis in collaboration between Ericsson and Chalmers. Their support, encouragement, and guidance throughout the project have been highly appreciated and have made this experience both valuable and rewarding.

Christoffer Lennernäs, Gothenburg, June 2026
Rasmus Gyllenhammar, Gothenburg, June 2026

Division of Work

This thesis was carried out as a collaborative effort, with both authors contributing to all major aspects of the project throughout, including problem formulation, technical development, problem-solving, literature review, analysis, discussions, and the writing and review of the thesis.

While the majority of the work was carried out jointly, certain tasks were divided according to the authors' primary areas of responsibility. Christoffer Lennernäs was primarily responsible for the development and implementation of the ray-tracing and feed models, as well as the sections of the thesis covering the underlying electromagnetic theory. Rasmus Gyllenhammar was primarily responsible for result generation, testing, validation of the Physical Optics (PO) implementation, and performance evaluation of the developed methods. He also took primary responsibility for the corresponding sections of the thesis related to these topics.

List of Acronyms

Below is the list of acronyms that have been used throughout this thesis listed in alphabetical order:

AUT	Antenna Under Test
CATR	Compact Antenna Test Range
DUT	Device Under Test
DT	Digital Twin
EFIE	Electric Field Integral Equation
FDTD	Finite Difference Time Domain
FEM	Finite Element Method
MFIE	Magnetic Field Integral Equation
MoM	Method of Moments
OTA	Over-The-Air
PEC	Perfect Electric Conductor
GO	Geometrical Optics
PO	Physical Optics
PTD	Physical Theory of Diffraction
QZ	Quiet Zone
RF	Radio Frequency
RWG	Rao-Wilton-Glisson
XPD	Cross-polar Discrimination

Nomenclature

Notation

$\mathbf{B}$	Magnetic flux density
$\mathbf{E}$	Electric field
$\mathbf{H}$	Magnetic field
$\mathbf{D}$	Electric flux density
$\mathbf{J}$	Electric current density
$\mathbf{J}_s$	Electric surface current density
ρ	Electric charge density
ρ_s	Surface electric charge density
μ	Permeability
ϵ	Permittivity
σ	Electrical conductivity
λ	Wavelength
$\mathbf{A}$	Vector potential
Φ	Scalar potential
j	Imaginary unit

Contents

List of Figures

List of Tables

1

Introduction

1.1 Background

Wireless communication systems and antenna technologies rely on accurate measurement techniques for evaluation and verification. One widely used approach is over-the-air (OTA) testing, where antennas and wireless devices are characterized under conditions that emulate free-space electromagnetic propagation. A common OTA measurement environment is the Compact Antenna Test Range (CATR) chamber, which is designed to generate a plane-wave field within a defined measurement region referred to as the Quiet Zone (QZ). A key performance parameter in a CATR chamber is the quality of the QZ, where the electromagnetic field should approximate a uniform plane wave with limited amplitude and phase variations. However, unintended scattering from objects inside the chamber may distort the QZ and negatively affect measurement accuracy [1]. Evaluating such effects experimentally can be time-consuming and resource intensive, especially in industrial environments where chamber availability is limited and measurements are tightly scheduled. Consequently, simulation-based methods are of increasing interest for supporting chamber analysis and troubleshooting [2].

A Digital Twin (DT) is a virtual representation of a physical system or process that maintains a synchronized relationship with its physical counterpart through measurement data, sensor information, and computational models [3, 4]. Digital twins are used in a wide range of applications including system monitoring, visualization, predictive maintenance, optimization, and simulation of system behavior under varying operating conditions [4].

For electromagnetic measurement environments such as Compact Antenna Test Range (CATR) chambers, a DT can provide a virtual platform for analysis and evaluation of chamber performance. Such a model can support virtual verification of measurement setups, optimization of measurement procedures and positioning systems, monitoring of mechanical and thermal conditions, and predictive maintenance of chamber components. In addition, the DT may enable investigation of electromagnetic phenomena including reflections, diffraction, scattering effects, noise contributions, and QZ degradation prior to physical implementation or testing.

The long-term objective of this work is the development of a high-fidelity DT of the OTA chamber used for evaluation and verification of wireless communication

systems and antenna technologies. The envisioned DT framework aims to combine simulation models, sensor data, and chamber characterization measurements to create a modular and continuously updated representation of the chamber environment. As an initial step toward this objective, this thesis focuses on the development and evaluation of a simulation model of the CATR chamber, with particular emphasis on investigating how scattering objects influence the electromagnetic field distribution and QZ characteristics.

1.2 Aims and objectives

The aim of this thesis is to develop and evaluate a simulation representation of the Ericsson OTA chamber and investigate how scattering objects and chamber configurations influence QZ characteristics.

This thesis addresses the following objectives:

- Evaluate the extent to which a simulation chamber model can reproduce the qualitative QZ field behavior consistent with physical OTA chamber behavior.
- Investigate how amplitude ripple, phase ripple, and total amplitude/phase variation in the QZ are affected by the presence of a scattering object.
- Identify limitations and sources of uncertainty within the simulation model that influence the calculated QZ metrics.
- Assess whether the developed chamber model can be used to comparatively evaluate QZ degradation caused by scattering objects.
- Examine how the developed simulation framework can contribute to digital-twin-based analysis and evaluation of OTA chambers.

1.3 Delimitations

Due to modeling complexity and computational constraints, several simplifications were introduced

- The chamber walls are modeled as free space, meaning that absorber structures present in the physical OTA chamber are not included. Accurate modeling of absorber reflections and material behavior is outside the scope of this work and constitutes a separate research problem.
- Thermal and mechanical effects are neglected.
- Direct radiation from the feed antenna to the QZ is neglected in the simulation model.
- Only the dominant propagation and scattering mechanisms relevant to the investigated scenarios are considered.

2

Theory

This chapter introduces the electromagnetic and antenna-measurement theory needed to understand the modelling approach used in this thesis.

2.1 Antenna Measurement Sites

Antenna measurement sites are used to evaluate antenna performance and to verify that antennas satisfy specified design requirements. The antenna being evaluated is commonly referred to as the Antenna Under Test (AUT) or Device Under Test (DUT). In antenna measurements, an additional antenna with known characteristics is typically required to transmit or receive electromagnetic waves during the characterization process. This antenna is commonly referred to as a source antenna, feed or reference antenna, depending on the measurement configuration. By exciting the AUT with a known electromagnetic field, parameters such as radiation pattern, gain, and polarization can be accurately determined [1, 5].

Accurate antenna testing and characterization require measurement environments that closely resemble free-space conditions. In practical measurements, reflections from surrounding objects, floors, walls, and external electromagnetic interference can significantly affect the measured antenna parameters such as radiation pattern, gain, directivity, and polarization. Antenna measurement sites are therefore designed to minimize unwanted reflections and external disturbances while providing controlled electromagnetic conditions. Common antenna measurement facilities include outdoor far-field ranges, anechoic chambers, and Compact Antenna Test Ranges (CATRs) [5].

To perform antenna measurements, the AUT must be illuminated by a uniform plane wave. Under plane-wave conditions, the wavefront is uniform and ensures that the measured antenna response is independent of the separation distance between the antennas. If the AUT is less than the Fraunhofer far-field distance, spherical wavefront effects and phase variations across the antenna aperture may introduce measurement errors and distort the measured radiation characteristics. Therefore, the AUT should be located in the far-field region of the transmitting antenna, where the Fraunhofer condition is satisfied. The far-field criterion is given by

$$r \geqslant \frac{2D^2}{\lambda}, \tag{2.1}$$

where D is the largest dimension of the larger of the two antennas and λ is the wavelength [1, 5].

2.1.1 Anechoic Chambers

An anechoic chamber is a shielded enclosure designed to suppress electromagnetic reflections and simulate free-space propagation conditions. The inner surfaces are typically covered with Radio Frequency (RF) absorbing material, often in the form of pyramidal absorbers. Reflections on these absorbers increase as the angle of incidence increases. They act, in effect, as a tapered impedance, where the wave gradually weakens with each reflection between the pyramids. By the time the wave reaches the end of the chamber's wall, the impedance transition is smooth so that there there are minimal reflections back toward the source of the field [1, 5].

As a result, anechoic chambers enable antenna measurements with improved accuracy and repeatability. However, for electrically large antennas, the far-field distance requirement given in (2.1) may exceed the physical dimensions of practical chambers, which motivates the use of Compact Antenna Test Ranges (CATRs) [1, 5].

2.1.2 Compact Antenna Test Ranges

A Compact Antenna Test Range (CATR) enables measurement of electrically large antennas at significantly reduced distances compared to conventional far-field ranges. For high-frequency or large-aperture antennas, the far-field condition in (2.1) may require separation distances on the order of tens or hundreds of meters, which is often impractical [1].

A CATR overcomes this limitation by using a parabolic reflector inside an anechoic chamber to transform a spherical wave emitted by the source antenna (feed). When the feed antenna is positioned at the focal point of the reflector, the reflected rays collimate, producing approximately a plane wave in the test region. In this configuration, equal ray path lengths from the feed through the reflector to the test zone ensure a close to uniform phase across the aperture, resulting in a well-defined plane-wave illumination of the AUT [1, 5].

2.1.2.1 Quiet Zone and Performance Metrics

The electromagnetic field reflected by the parabolic reflector is evaluated in a region commonly referred to as the test zone or QZ. Within this region, a central portion exhibits approximately planar wavefronts with sufficiently uniform amplitude and phase characteristics. This region is defined as the QZ, and it represents the effective measurement area in which the AUT is placed [1, 5].

The performance of a CATR is typically characterized using several performance metrics, including phase deviation, amplitude ripple and amplitude taper. These parameters describe the deviation of the generated field from an ideal plane wave within the QZ [1, 5].

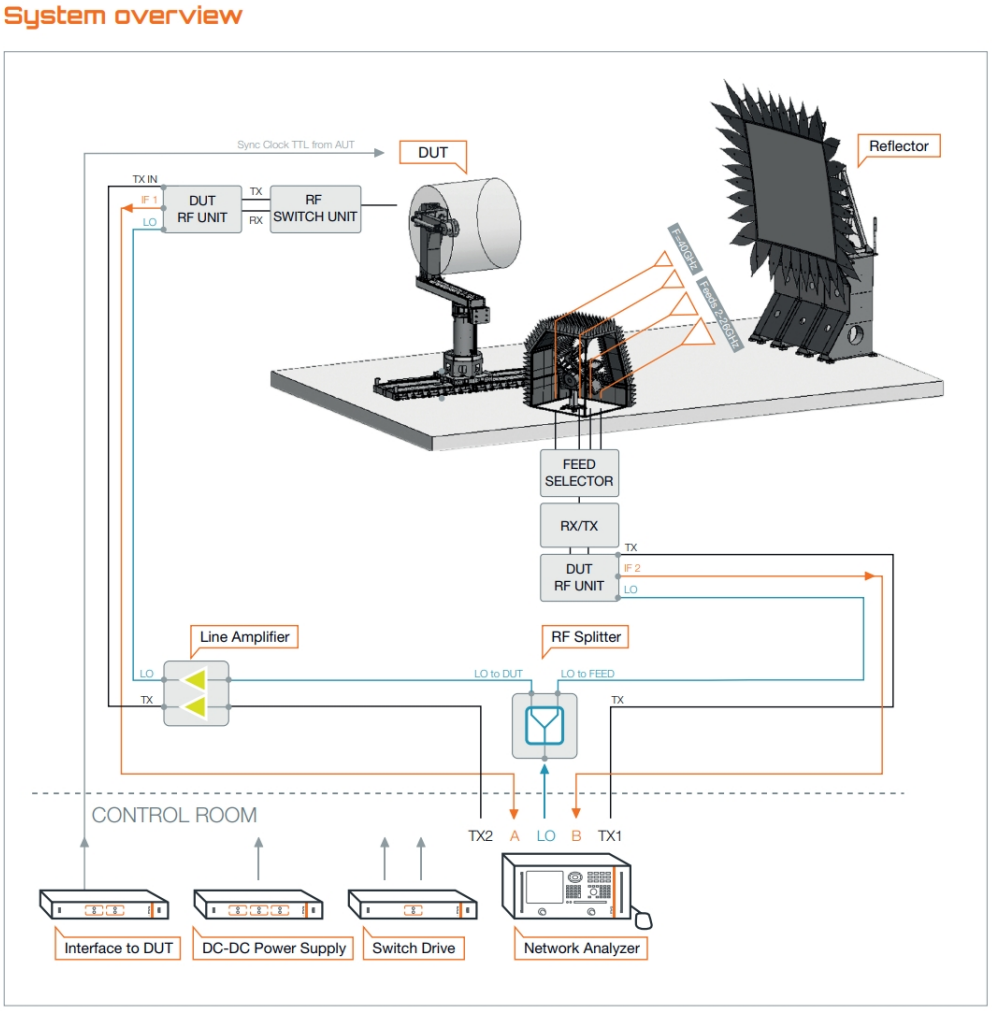

Figure 2.1: System overview of the compact antenna test range (CATR) measurement setup, showing the reflector, feed system, DUT positioning, RF signal routing, and control-room instrumentation used for OTA characterization. Courtesy MVG.

According to Balanis [1], in most practical antenna measurement applications, phase deviations below 10°, peak-to-peak amplitude ripple below 1 dB, and amplitude taper below 1 dB are considered acceptable performance levels. Maintaining phase and amplitude variations within these limits reduces distortions in the measured antenna characteristics. These performance metrics are affected by several factors. The amplitude taper is due to radiation pattern by source antenna and free space loss factor [1].

The diffraction responsible for the ripple in the QZ originates primarily from the edges of the reflector. To mitigate this effect, serrated edges, as shown on the reflector in Fig. 2.1, are employed to reduce the amplitude and phase coherence of the diffracted fields. Serrated reflector edges generate multiple low-amplitude diffraction contributions that are randomized in amplitude, phase, and polarization [1]. The

ripple period can be determined by

$$T_{\text{ripple}} = \frac{\lambda}{\sin(\alpha)} \tag{2.2}$$

where α is the direction angle relative to boresight.

2.2 Polarization

Polarization describes the orientation of the electric field vector of an electromagnetic wave. It can be decomposed into a co-polarized component and a cross-polarized component. The co-polarized component represents the desired electric field component and the cross-polarized component is the unwanted electric field component. These components are denoted by E_{co} and E_{xp} and are directed along the unit vectors $\hat{\mathbf{co}}$ and $\hat{\mathbf{xp}}$ [6].

Several types of polarization exist, including linear and circular polarization [6]. According to Ludwig's first definition, it states that the co-polarized and cross-polarized components are obtained by projecting the electric field onto two orthogonal cartesian unit vectors, such as $\hat{\mathbf{x}}$ and $\hat{\mathbf{y}}$ [7, 8]. For example, if the wave propagates in the $\hat{\mathbf{z}}$ direction and the desired polarization is aligned with the x-axis, the polarization basis vectors are defined as [6].

$$\hat{\mathbf{co}} = \hat{\mathbf{x}} \qquad \text{and} \qquad \hat{\mathbf{xp}} = \hat{\mathbf{y}}. \tag{2.3}$$

The corresponding polarization components of the electric field are then given by

$$E_{\text{co}} = \mathbf{E} \cdot \hat{\mathbf{co}}^* = \mathbf{E} \cdot \hat{\mathbf{x}}^* = E_x, \tag{2.4a}$$
$$E_{\text{xp}} = \mathbf{E} \cdot \hat{\mathbf{xp}}^* = \mathbf{E} \cdot \hat{\mathbf{y}}^* = E_y. \tag{2.4b}$$

In this work, Ludwig's first definition is used to determine the co-polarized and cross-polarized components.

The cross-polarization level can be quantified using the cross-polar discrimination (XPD) metric. XPD is the ratio of the co-polar component compared to the orthogonal cross-polar component and is defined as

$$(\text{XPD})_{\text{dB}} = 10 \log \left| \frac{E_{\text{co}}}{E_{\text{xp}}} \right|^2 \tag{2.5}$$

Consequently, a higher XPD value indicates greater polarization purity [6].

2.3 Maxwell's Equations

Maxwell's equations form the foundation of classical electromagnetic theory, describing how electric and magnetic fields are generated and interact with charges

and currents. In differential form, they are given by [9]:

$$\nabla \times \mathbf{E} = -\frac{\partial \mathbf{B}}{\partial t} \tag{2.6a}$$

$$\nabla \times \mathbf{H} = \mathbf{J} + \frac{\partial \mathbf{D}}{\partial t} \tag{2.6b}$$

$$\nabla \cdot \mathbf{D} = \rho \tag{2.6c}$$

$$\nabla \cdot \mathbf{B} = 0 \tag{2.6d}$$

Here, $\mathbf{E}$ denotes the electric field, $\mathbf{H}$ the magnetic field, $\mathbf{D}$ the electric flux density, and $\mathbf{B}$ the magnetic flux density. The quantity $\mathbf{J}$ represents the electric current density, and ρ the electric charge density.

2.4 Boundary Conditions of Different Media

When solving for the electric field distribution in a system with multiple media (see Fig. 2.2), abrupt changes (step discontinuities) in material properties, such as at the boundary between two materials, make the field non-differentiable since the derivatives would imply an infinite rate of change [10].

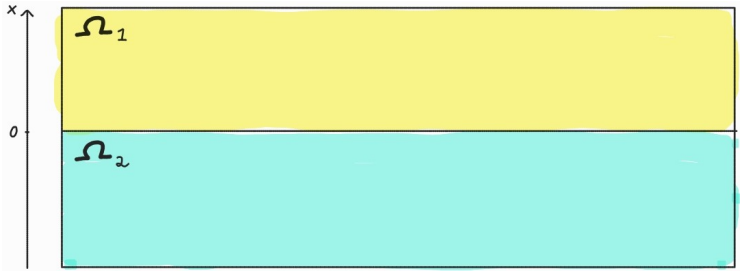

Figure 2.2: Schematic of two media, Ω_1 and Ω_2 separated by the boundary at $x = 0$.

To handle this, instead treat each medium as a separate homogeneous region where the governing differential equations remain well-defined. The boundary between the media is then handled by introducing appropriate boundary conditions. Under the assumption of no surface charge, these conditions ensure matching conditions between the fields on both sides of the boundary, allowing the solution for the electric field to be determined throughout the entire domain.

In this way, the problem is reformulated as multiple homogeneous regions connected through boundary conditions, rather than a single inhomogeneous system.

Therefore, the electromagnetic boundary equations will be derived using Maxwell's equations in integral form for electrostatics, i.e

In this way, the problem is reformulated as multiple homogeneous regions connected through boundary conditions, rather than a single inhomogeneous system. These interface conditions can be derived from Maxwell's equations in integral form. In

particular, the boundary condition for the tangential component of the electric field is obtained from Faraday's law, which in integral form is given by

Faraday's law: $\oint_L \mathbf{E} \cdot d\mathbf{l} = 0$ $\Rightarrow$ Boundary conditions for tangential component of electric fields

Consider the interface between two different media ϵ_1 and ϵ_2, in this case ϵ_2 is a Perfect Electric Conductor (PEC) (see Fig. 2.3a). The goal is to determine the relationship between the electric fields on either side of the interface, so that knowing the field in one medium allows us to determine the field in the other region.

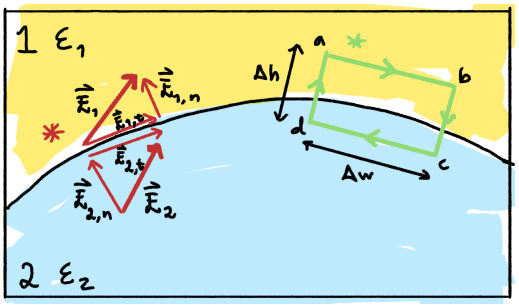

(a) Two media with their respective electric field and a closed path around the boundary in green.

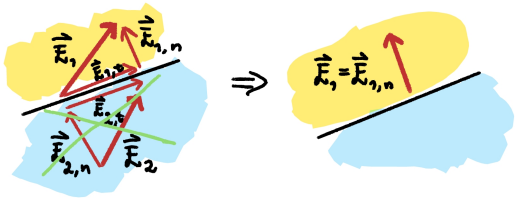

(b) The yellow medium has finite conductivity, while the blue medium is a PEC. The figure shows the resulting electric field distribution under these conditions.

Figure 2.3: Illustration of the boundary conditions at the interface between a medium and a PEC.

To do this, it is useful to decompose the electric field on each side of the interface into its normal and tangential components, see the red asterisk * in Fig. 2.3a.

Apply the following integral to a closed path spanning some section of the boundary, see green asterisk * in Fig. 2.3a. Using Faraday's law it can be shown that

$$0 = \oint_L \mathbf{E} \cdot d\mathbf{l} \implies \mathbf{E}_{1,t} = \mathbf{E}_{2,t} \tag{2.7}$$

meaning that the tangential electric field at the boundary must be the same for both media. For the full derivation can be found in appendix A. Now recall Ohm's law in vector form

$$\mathbf{J} = \sigma \mathbf{E} \tag{2.8}$$

Consider the case where region 2 is a PEC then the conductivity becomes unbounded, $\sigma \to \infty$. From Ohm's law, two formal possibilities arise: either the electric field inside the PEC $\mathbf{E} \neq 0$ and the current density $\mathbf{J}$ diverges, or the electric field $\mathbf{E} = 0$ inside the PEC and $\mathbf{J}$ converges.

A more rigorous treatment, obtained by examining the limiting behavior of σ and $\mathbf{E}$, shows that the physically consistent solution is the latter. That is, the electric field inside a PEC must be zero, $\mathbf{E} = 0$. Consequently, the current density remains finite rather than diverging.

Intuitively, this result is also consistent with physical reality: materials that approximate a PEC do not exhibit unbounded currents in response to finite applied fields. Instead, free charges redistribute instantaneously to cancel the internal electric field.

From Fig. 2.3b, by enforcing that the electric field inside the PEC vanishes, the tangential component of the electric field in medium ϵ_2 must be zero. According to (2.7), this implies that the tangential electric field in the adjacent medium ϵ_1 at the interface must also vanish. Therefore, the tangential component of the electric field at the interface is zero, and only a normal component of the electric field can exist at the boundary.

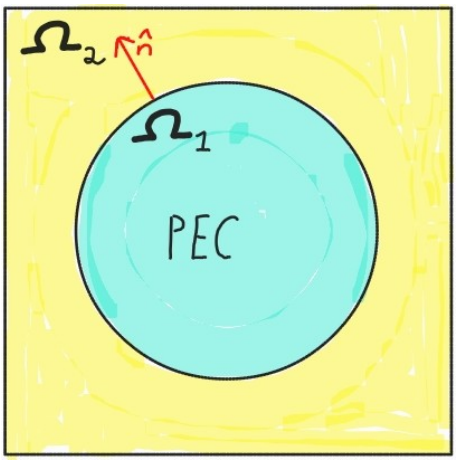

Figure 2.4: Closed surface divided into a yellow region Ω_2 with finite conductivity and a blue region Ω_1 that is a PEC. The red arrow represents the normal vector $\hat{\mathbf{n}}$ on the interface.

Let a closed surface S divide into two regions, Ω_1 and Ω_2, with Ω_1 representing the region enclosed by S and Ω_2 the surrounding region. Let the normal vector $\hat{\mathbf{n}}$ be perpendicular to the surface S, pointing towards Ω_2, see Fig. 2.4. Assuming that Ω_1 is a PEC, the boundary conditions simplify to the following [9].

$$\hat{\mathbf{n}} \times \mathbf{E}_2 = 0 \tag{2.9a}$$

$$\hat{\mathbf{n}} \times \mathbf{H}_2 = \mathbf{J}_s \tag{2.9b}$$

$$\hat{\mathbf{n}} \cdot \mathbf{D}_2 = \rho_s \tag{2.9c}$$

$$\hat{\mathbf{n}} \cdot \mathbf{B}_2 = 0 \tag{2.9d}$$

Under PEC boundary conditions, all the fields inside the PEC region are zero. This provides a good approximation for metallic surfaces [9, 11].

2.5 Computational Electromagnetic Solvers

Computational electromagnetics (CEM) comprises numerical methods used to solve Maxwell's equations for realistic structures and material configurations that are not easily managed by analytical methods. In scattering problems, an incident field interacts with an object and produces induced currents which in turn give rise to scattered fields. The total field is then obtained from the superposition of the incident and scattered contributions. A wide range of numerical techniques has been developed for this purpose and in this section four commonly used methods are considered [12].

2.5.1 Finite Element Method - FEM

The Finite Element Method (FEM) is a widely used numerical technique for solving differential equations in several fields, including electromagnetics. FEM is a

method that requires discretization of the entire volumetric computational domain into smaller elements, commonly tetrahedral or triangular meshes. This discretization enables accurate modeling of complex geometries and inhomogeneous materials [13].

FEM transforms Maxwell's equations into a system of linear equations that is solved numerically. FEM provides high accuracy and geometric flexibility, making it well suited for complex structures and material configurations. However, the volumetric discretization results in a large number of linear equations, leading to high memory usage and computational cost for electrically large problems [14].

2.5.2 Finite Difference Time Domain - FDTD

The finite-difference time-domain (FDTD) method is a numerical technique used to model electromagnetic problems. Similar to FEM, FDTD is a volumetric method that requires discretization of the entire computational domain. The method solves Maxwell's time-dependent curl equations directly by discretizing both space and time, where the electromagnetic field components are computed iteratively at each time step [15, 16].

An advantage of FDTD is that it avoids solving large systems of linear equations. However, the time-step size is restricted by numerical stability conditions and the smallest discretization element in the model. This results in a large number of time steps for fine geometries, increasing the overall computational cost. Consequently, FDTD becomes less efficient for electrically large problems and structures containing fine geometric details [17]. FDTD also gives rise to late-time instabilities due to round-off errors that accumulate [13].

2.5.3 Physical Optics - PO

Physical Optics (PO) is a high-frequency approximation method used to estimate scattering from electrically large, smooth conducting structures and it lies between Geometrical Optics (GO) and full-wave electromagnetic analysis. The PO uses the incident field to approximate the induced currents on the surface, avoiding the need to solve large coupled systems of equations [18, 19].

Since the method only evaluates currents on the illuminated region of the surface, PO is computationally efficient and particularly suitable for large reflector structures. However, the approximation neglects diffraction and consequently, it reduces the accuracy especially around edges of the structures [19].

Based on the characteristics of electrically large reflector structures operating at high frequencies, PO is well suited for modeling the CATR reflector [1].

2.5.3.1 Physical Optics Formulation

Assume that an infinite flat PEC surface is illuminated by an incident field $\mathbf{E}^i$ and the resulting scattered field $\mathbf{E}^s$, then the PEC boundary conditions (2.9a) and (2.9b)

together for an infinite plane yield [19]:

$$\mathbf{E}_{\tan} = \mathbf{E}^i_{\tan} + \mathbf{E}^s_{\tan} = 0 \tag{2.10}$$

and

$$\mathbf{H}_{\tan} = \mathbf{H}^i_{\tan} + \mathbf{H}^s_{\tan} = 2\mathbf{H}^i_{\tan} \tag{2.11}$$

at the surface. Applying the result in (2.9b) to (2.11) produces the PO surface current stated as [19]:

$$\mathbf{J}_s = \hat{\mathbf{n}} \times (\mathbf{H}^i + \mathbf{H}^s) = 2\hat{\mathbf{n}} \times \mathbf{H}^i, \tag{2.12}$$

where $\hat{\mathbf{n}}$ is chosen as the outward normal from the illuminated PEC surface, pointing toward the incident-field region.

In addition, for finite smoothly curved PEC bodies, PO extends this result by applying the PO current distribution locally over tangent planes with infinite extent [19]. On the backside of the surface, PO assumes no illumination following GO and thus the induced surface current is defined as $\mathbf{J}_s = 0$.

$$\mathbf{J}_s = \begin{cases} 2\hat{\mathbf{n}} \times \mathbf{H}^i, & \text{illuminated side} \\ 0, & \text{non-illuminated side} \end{cases} \tag{2.13}$$

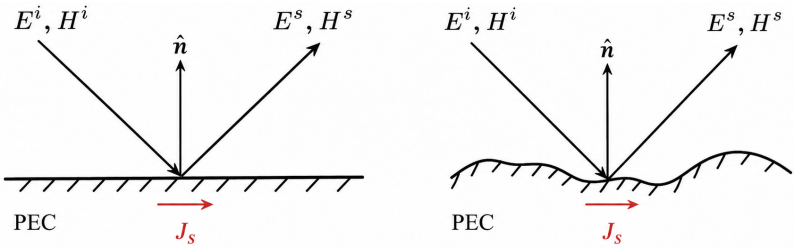

Figure 2.5: An incident field $\mathbf{E}^i$ and, $\mathbf{H}^i$ illuminates a PEC. (a) Infinite, flat conductor. (b) Finite smoothly curved conductor.

The final expression (2.13) can be used to calculate electric scattered fields from large finite, curved bodies.

2.5.4 Method of Moments - MoM

The Method of Moments (MoM) is a full-wave numerical technique used to solve electromagnetic scattering and radiation problems by reformulating Maxwell's equations into integral equations. Unlike methods such as the Finite Element Method (FEM) and Finite-Difference Time-Domain (FDTD), MoM is based on surface integral equations and requires discretization only of the object surface [13].

Because Green's function in the MoM formulation naturally satisfies the radiation condition, ensuring that electromagnetic fields decay proportionally to $1/r$ in free space, it is particularly well-suited for radiation and scattering problems involving conducting structures [13].

However, MoM results in a dense system matrix, which leads to high memory consumption and computational cost. The method therefore becomes less practical for electrically large problems [13].

For smaller radiation and scattering objects within the chamber, a full-wave approach such as MoM is more appropriate due to its higher accuracy in modeling smaller geometries and highly conducting surfaces [13].

2.5.4.1 Method of Moments Formulation

A more detailed formulation of MoM begins by expressing the scattered electromagnetic fields in terms of equivalent surface currents. Unlike PO, which treats each illuminated surface independently, MoM enforces boundary conditions over the entire geometry simultaneously.

The geometry is discretized into small mesh elements, as illustrated in Fig. 2.6, and the induced surface current is expanded using a set of basis functions defined on these elements. The resulting system of equations is then solved to determine the unknown current coefficients, which are subsequently used to compute the scattered electromagnetic fields.

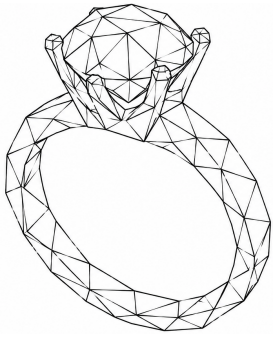

Figure 2.6: Low-polygon surface discretization of a ring using triangular facets.

Let the unknown surface current density $\mathbf{J}_s(\mathbf{r})$ be expressed as

$$\mathbf{J}_s(\mathbf{r}) = \sum_{n=1}^{N} I_n \mathbf{f}_n(\mathbf{r}), \tag{2.14}$$

where $\mathbf{f}_n$ are chosen basis functions and I_n are unknown coefficients and N is the number of basis functions. Fig. 2.7 illustrates the source and observation point geometry used in the formulation.

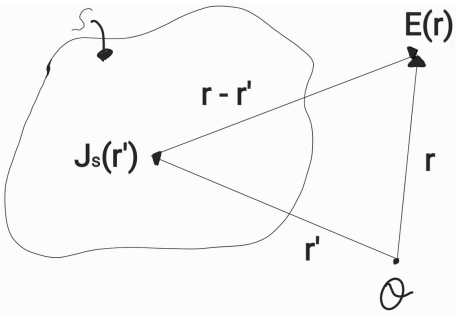

Figure 2.7: Source point $\mathbf{r}'$, observation point $\mathbf{r}$, and separation vector $\mathbf{r} - \mathbf{r}'$.

The integral equation is then enforced in a weighted sense by testing it against a set of functions w_m. This procedure transforms the continuous problem into a system of linear equations,

$$\sum_{n=1}^{N} Z_{mn} I_n = V_m, \tag{2.15}$$

where Z_{mn} represents the interaction between basis and testing functions, and V_m represents the excitation.

Solving this matrix equation yields the coefficients I_n, which approximate the original unknown function. MoM is particularly well-suited for problems involving conducting surfaces, especially perfect electric conductors, where it is used to compute surface current distributions.

2.5.4.2 Electric Field Integral Equation

If the point $\mathbf{r}$ lies on the conducting surface S, the PEC boundary condition states that

$$\mathbf{J}_s = \hat{\mathbf{n}} \times \mathbf{H}, \tag{2.16}$$

where $\mathbf{J}_s$ is the induced surface current density, $\hat{\mathbf{n}}$ is the unit normal vector to the surface, and $\mathbf{H}$ is the magnetic field at the surface. Applying this boundary condition to the magnetic field representation leads to the magnetic field integral equation (MFIE). The MFIE can be derived from the magnetic-field representation, however, since the surface-current solution used in this thesis is based on the Electric Field Integral Equation (EFIE), only the EFIE formulation is presented in detail.

As previously shown, the tangential electric field vanishes on a PEC surface, i.e., $\mathbf{E}_{\tan} = 0$, this boundary condition leads to an EFIE. By the equivalence principle and linearity, the total electric field can be written as $\mathbf{E} = \mathbf{E}^i + \mathbf{E}^s(\mathbf{J}_s)$.

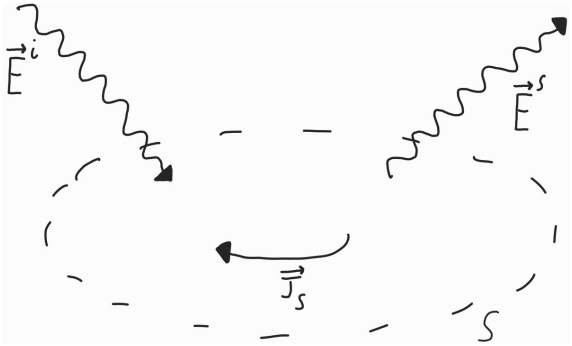

Figure 2.8: The incident electric field $\vec{E}^i$ induces an equivalent surface current density $\vec{J}_s$, which radiates the scattered electric field $\vec{E}^s$.

The surface current density $\mathbf{J}_s$ is determined such that the scattered field $\mathbf{E}_s$, together with the incident field $\mathbf{E}_i$ as illustrated in Fig. 2.8, satisfies the boundary condition of zero tangential electric field on the surface S. Since the electric field is expressed as a function of $\mathbf{J}_s$, the problem can be solved for the surface current density through Faraday's law in (2.6a) and Gauss's law for magnetism in (2.6d).

$$\nabla \times \mathbf{E} + \frac{\partial \mathbf{B}}{\partial t} = 0 \tag{2.17}$$

$$\nabla \cdot \mathbf{B} = 0 \tag{2.18}$$

To simplify the solution of the Electric Field Integral Equation (EFIE), scalar and vector potentials are introduced. The scalar and vector potentials satisfy the following vector identities:

$$\nabla \times (\nabla \Phi) = 0, \tag{2.19}$$

$$\nabla \cdot (\nabla \times \mathbf{A}) = 0, \tag{2.20}$$

Proofs of these identities are provided in Appendix B. The first identity states that the curl of a gradient always vanishes, implying that conservative fields may be written in terms of a scalar potential Φ. The second identity states that the divergence

of a curl always vanishes, which allows divergence-free fields to be expressed in terms of a vector potential $\mathbf{A}$.

As Gauss's law for magnetism in (2.6d) states that magnetic monopoles do not exist, the divergence of the magnetic field is identically zero. Consequently, the magnetic field can only possess a rotational component and may therefore be expressed as the curl of a vector potential $\mathbf{A}$,

$$\mathbf{B} = \nabla \times \mathbf{A}. \tag{2.21}$$

Taking the divergence of both sides and using (2.20) (or (2.6d)) yields

$$\nabla \cdot \mathbf{B} = \nabla \cdot (\nabla \times \mathbf{A}) = 0. \tag{2.22}$$

Substituting $\mathbf{B} = \nabla \times \mathbf{A}$ into Faraday's law,

$$\nabla \times \mathbf{E} + \frac{\partial}{\partial t}(\nabla \times \mathbf{A}) = 0. \tag{2.23}$$

Because spatial and time derivatives commute,

$$\nabla \times \left(\mathbf{E} + \frac{\partial \mathbf{A}}{\partial t} \right) = 0. \tag{2.24}$$

Since the curl of the quantity inside the parentheses is zero, it can be expressed as the gradient of a scalar potential. Introducing the scalar potential Φ gives

$$\nabla \times \underbrace{\left(\mathbf{E} + \frac{\partial \mathbf{A}}{\partial t} \right)}_{=-\nabla\Phi} = 0 \quad \Rightarrow \quad \mathbf{E} + \frac{\partial \mathbf{A}}{\partial t} = -\nabla\Phi. \tag{2.25}$$

where the minus sign is introduced by convention. Rearranging gives the electric field in terms of the scalar and vector potentials:

$$\mathbf{E} = -\frac{\partial \mathbf{A}}{\partial t} - \nabla\Phi. \tag{2.26}$$

Now assume a time-harmonic wave and suppress the time dependence. The electric field created by the surface current density $\mathbf{J}_s$ is

$$\mathbf{E}_s(\mathbf{J}_s) = -j\omega\mathbf{A} - \nabla\Phi \tag{2.27}$$

For a PEC surface, the tangential component of the total electric field must vanish:

$$(\mathbf{E}^i + \mathbf{E}^s)_{\tan} = 0, \qquad \mathbf{r} \in \mathbf{S} \tag{2.28}$$

Hence,

$$\mathbf{E}^i_{\tan} = -\mathbf{E}^s_{\tan} = (j\omega\mathbf{A} + \nabla\Phi)_{\tan}, \qquad \mathbf{r} \in \mathbf{S} \tag{2.29}$$

Using the Green's function formulation, the vector potential $\mathbf{A}$ and scalar potential Φ can be expressed as [1]

$$\mathbf{A}(\mathbf{r}) = \mu \iint \mathbf{J}_s(\mathbf{r}')\, G(\mathbf{r} - \mathbf{r}')\, dS' \tag{2.30}$$

$$\Phi(\mathbf{r}) = -\frac{1}{j\omega\epsilon} \iint \nabla' \cdot \mathbf{J}_s(\mathbf{r}')\, G(\mathbf{r} - \mathbf{r}')\, dS' \tag{2.31}$$

where the Green's function is given by

$$G(\mathbf{r}-\mathbf{r}') = \frac{e^{-jk|\mathbf{r}-\mathbf{r}'|}}{4\pi|\mathbf{r}-\mathbf{r}'|}. \tag{2.32}$$

Meaning (2.29) can be rewritten together with the function above as,

$$\mathbf{E}^i = j\omega\mu \iint \mathbf{J}_s(\mathbf{r}')\, G(\mathbf{r}-\mathbf{r}')\, ds' - \frac{1}{j\omega\epsilon}\nabla \iint \nabla'\cdot\mathbf{J}_s(\mathbf{r}')\, G(\mathbf{r}-\mathbf{r}')\, ds'. \tag{2.33}$$

This is the Electric Field Integral Equation (EFIE), where the surface current density $\mathbf{J}_s$ is the unknown quantity. In general, the integral equation due to its complexity is solved numerically.

2.5.4.3 Basis Functions

To obtain a numerical solution using the Method of Moments (MoM), as mentioned previously, the unknown current is approximated as a weighted sum of known basis functions

$$\mathbf{J}_s(\mathbf{r}) \approx \sum_{n=1}^{N} I_n \mathbf{f}_n(\mathbf{r}), \tag{2.34}$$

where $\mathbf{f}_n(\mathbf{r})$ are the basis functions and I_n are the unknown coefficients to be solved for [20].

The basis functions describe how the surface current flows locally across the geometry. For complex or non-planar structures such as Fig. 2.6, the current distribution may vary nonlinearly across the surface. Although each basis function is simple, resulting in a locally piecewise-linear current distribution, their weighted combination can accurately approximate more complicated current distributions.

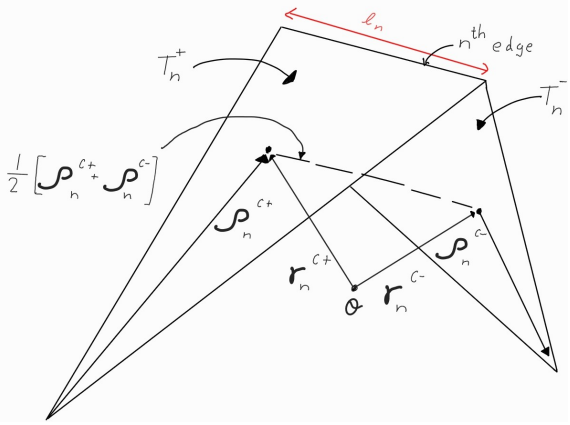

Figure 2.9: An RWG triangle patch pair consisting of two adjacent triangular elements, T_n^+ and T_n^-, sharing a common edge of length l_n.

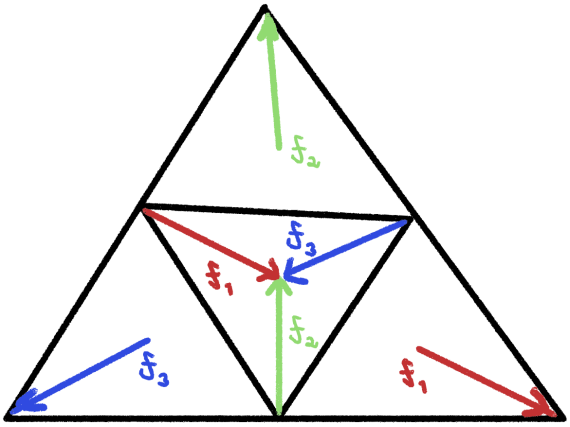

Figure 2.10: All triangle patch pairs for an arbitrary RWG triangle patch.

There are several types of basis functions available, and the one used in this thesis is the Rao-Wilton-Glisson (RWG) basis functions. RWG basis functions discretize the object into triangular elements, which makes them particularly suitable for modeling complex geometries.

The RWG basis functions are defined on pairs of adjacent triangles that share a common edge where the current can flow through [20]. The conducting structures

are represented by the RWG basis function as

$$\mathbf{f}_n(\mathbf{r}) = \begin{cases} \frac{l_n}{2A_n^+}\boldsymbol{\rho}_n^+, & \mathbf{r} \in T_n^+ \\ \frac{l_n}{2A_n^-}\boldsymbol{\rho}_n^-, & \mathbf{r} \in T_n^- \\ 0, & \text{otherwise} \end{cases} \tag{2.35}$$

where l_n is the common edge length between the triangle pair T_n^+ and T_n^-, and A_n^+ and A_n^- are the areas of the two triangles, respectively. Furthermore, $\boldsymbol{\rho}_n^+$ denotes the position vector from the free vertex of T_n^+ to a point within the triangle, while $\boldsymbol{\rho}_n^-$ denotes the position vector from a point within T_n^- to its free vertex, as illustrated in Fig. 2.9. These quantities are then used to calculate the surface charge density associated with a given triangle patch.

$$\nabla_S \cdot \mathbf{f}_n = \begin{cases} \frac{l_n}{A_n^+}, & \mathbf{r} \in T_n^+ \\ -\frac{l_n}{A_n^-}, & \mathbf{r} \in T_n^- \\ 0, & \text{otherwise} \end{cases} \tag{2.36}$$

The surface charge density is thus constant in each triangle and the total charge for T_n^+ and T_n^- is zero, one acts like a source and one as a sink.

The integrals over the triangular patches are then approximated using the midpoint integration rule, which leads to

$$\int_{\mathrm{T_n^+ + T_n^-}} \mathbf{f}_n \, dS = \frac{l_n}{2}(\boldsymbol{\rho}_n^{\mathrm{c}+} + \boldsymbol{\rho}_n^{\mathrm{c}-}) = l_n(\mathbf{r}_n^{\mathrm{c}+} - \mathbf{r}_n^{\mathrm{c}-}) \tag{2.37}$$

The reconstructed surface current on each triangle is obtained by summing the contributions of all RWG basis functions associated with its edges.

2.5.4.4 Solving the Electric Field Integral Equation

As introduced in (2.14), the surface current density can be approximated by a finite set of basis functions. The EFIE can be written compactly by introducing the linear operator L, which maps a surface current density to its scattered electric field,

$$\mathbf{E}^s_{\tan} = \big(L(\mathbf{J}_s)\big)_{\tan} = -\mathbf{E}^i_{\tan}. \tag{2.38}$$

The unknown surface current density is expressed using a finite set of basis functions

$$\mathbf{J}_s(\mathbf{r}') = \sum_{n=1}^{N} I_n \mathbf{f}_n(\mathbf{r}'), \tag{2.39}$$

where $\mathbf{f}_n$ are known basis functions and I_n are the unknown expansion coefficients. Substituting this approximation into the EFIE gives

$$\left(L\left(\sum_{n=1}^{N} I_n \mathbf{f}_n(\mathbf{r}') \right) \right)_{\tan} = -\mathbf{E}^i_{\tan}. \tag{2.40}$$

Since L is a linear operator, this can be written as

$$\left(\sum_{n=1}^{N} I_n L(\mathbf{f}_n)\right)_{\tan} = -\mathbf{E}^i_{\tan}. \tag{2.41}$$

This equation cannot be enforced exactly at every point on the surface using only a finite number of basis functions, hence it cannot be enforced exactly at every point. Therefore, an error must be allowed. The residual error is forced to be orthogonal to a set of testing functions $\mathbf{w}_m$. In Galerkin's method, the testing functions are chosen to be the same as the basis functions $\mathbf{w}_m = \mathbf{f}_m$. This gives

$$\iint_S \mathbf{w}_m(\mathbf{r}) \cdot \left[\sum_{n=1}^{N} I_n L(\mathbf{f}_n)\right] dS = -\iint_S \mathbf{w}_m(\mathbf{r}) \cdot \mathbf{E}^i(\mathbf{r})\, dS, \quad m = 1, 2, \ldots, N. \tag{2.42}$$

Moving the summation and coefficients outside the integral gives

$$\sum_{n=1}^{N} I_n \iint_S \mathbf{w}_m(\mathbf{r}) \cdot L(\mathbf{f}_n)\, dS = -\iint_S \mathbf{w}_m(\mathbf{r}) \cdot \mathbf{E}^i(\mathbf{r})\, dS. \tag{2.43}$$

We now define the matrix elements

$$Z_{mn} = \iint_S \mathbf{w}_m(\mathbf{r}) \cdot L(\mathbf{f}_n)\, dS \tag{2.44}$$

and the excitation vector

$$V_m = -\iint_S \mathbf{w}_m(\mathbf{r}) \cdot \mathbf{E}^i(\mathbf{r})\, dS. \tag{2.45}$$

The EFIE is therefore reduced to the matrix equation

$$\sum_{n=1}^{N} Z_{mn} I_n = V_m, \qquad m = 1, 2, \ldots, N. \tag{2.46}$$

In matrix form,

$$\mathbf{ZI} = \mathbf{V}, \tag{2.47}$$

where $\mathbf{Z}$ is the impedance matrix, $\mathbf{I}$ contains the unknown current coefficients, and $\mathbf{V}$ contains the excitation from the incident field. Solving this system gives

$$\mathbf{I} = \mathbf{Z}^{-1}\mathbf{V}. \tag{2.48}$$

This formulation reduces the continuous EFIE to a finite-dimensional matrix equation, allowing the unknown coefficients I_n to be solved numerically. Once these coefficients are known, the surface current density can be reconstructed from the basis function expansion (2.39). Thus, the induced surface current density on the PEC surface can be determined.

2.5.5 Calculation of the Electric and Magnetic Fields

The electric field $\mathbf{E}$ and magnetic field $\mathbf{H}$ are obtained from the source surface current density $\mathbf{J}_s(\mathbf{r}')$ through the magnetic vector potential $\mathbf{A}$. Starting from Maxwell's equations in a homogeneous medium and applying the Lorentz gauge condition [1]. Its solution can be expressed using the scalar Green's function

$$G(R) = \frac{e^{-jkR}}{4\pi R}, \tag{2.49}$$

where $R = |\mathbf{r} - \mathbf{r}'|$ is the distance between the observation point $\mathbf{r}$ and the source point $\mathbf{r}'$.

The magnetic vector potential is then calculated as defined in (2.30) which represents the superposition of the contributions from all source elements on the surface.

The magnetic field is obtained from the curl of the vector potential defined in (2.21), which yields the integral expression

$$\mathbf{H} = \int_S jk \left(1 + \frac{1}{jkR}\right) \left[\mathbf{J}_s(\mathbf{r}') \times \hat{\mathbf{R}}\right] G(R)\, dS'. \tag{2.50}$$

Similarly, the electric field is derived from the vector potential and the Lorentz gauge relation, resulting in

$$\mathbf{E} = \int_S -jk\eta \left[CN_1\, \mathbf{J}_s(\mathbf{r}') - CN_2\big(\mathbf{J}_s(\mathbf{r}') \cdot \hat{\mathbf{R}}\big)\hat{\mathbf{R}}\right] G(R)\, dS', \tag{2.51}$$

where

$$CN_1 = \left(1 + \frac{1}{jkR} - \frac{1}{(kR)^2}\right), \tag{2.52}$$

and

$$CN_2 = \left(1 - \frac{3}{(kR)^2} + \frac{3}{jkR}\right). \tag{2.53}$$

These coefficients account for the distance-dependent near-field and far-field contributions.

2.6 Elementary current for radiation

Incremental current sources are used to construct more complex sources by combining many small incremental sources [21]. This works because Maxwell's equations are linear, which allows the use of the superposition principle. As a result, the total field can be found by adding together the contributions from individual incremental sources. In this thesis three different incremental sources are considered:

1. An incremental electric current source or Hertz dipole is like an electric dipole that has both front and back radiation [22], seen in Fig. 2.11.
2. An incremental magnetic current source produces the same field pattern as an incremental electric current source but with the electric and magnetic fields interchanged [23], as illustrated in Fig. 2.12.
3. An Huygens source combines an electric and a magnetic dipole with appropriate amplitude and phase relationships such that the radiation in the backward direction is cancelled, resulting in an unidirectional elementary source [6].

For the numerical implementation, the continuous integrals in (2.50) and (2.51) are evaluated as discrete sums over incremental dipole sources.

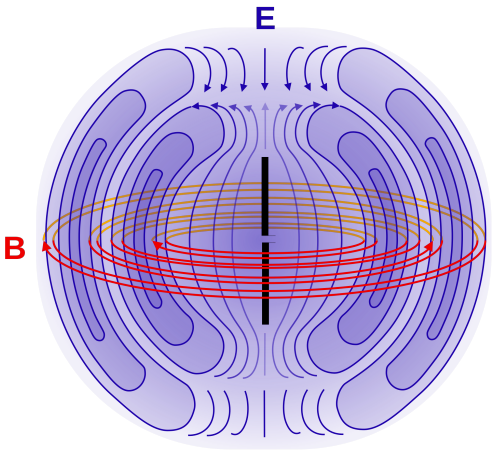

Figure 2.11: Electric dipole [24].

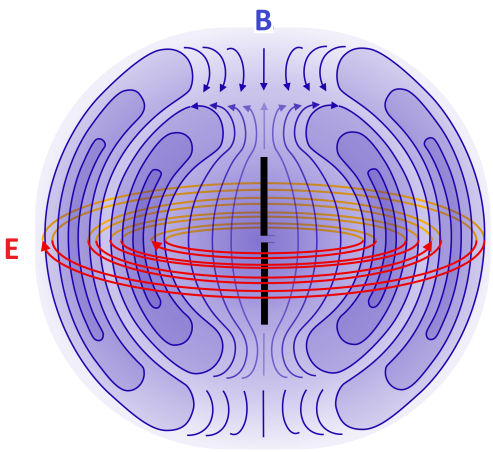

Figure 2.12: Magnetic dipole [24].

3

Methods

This chapter describes the main parts of the implementation of the electromagnetic solver part of the model. The following shows the system overview:

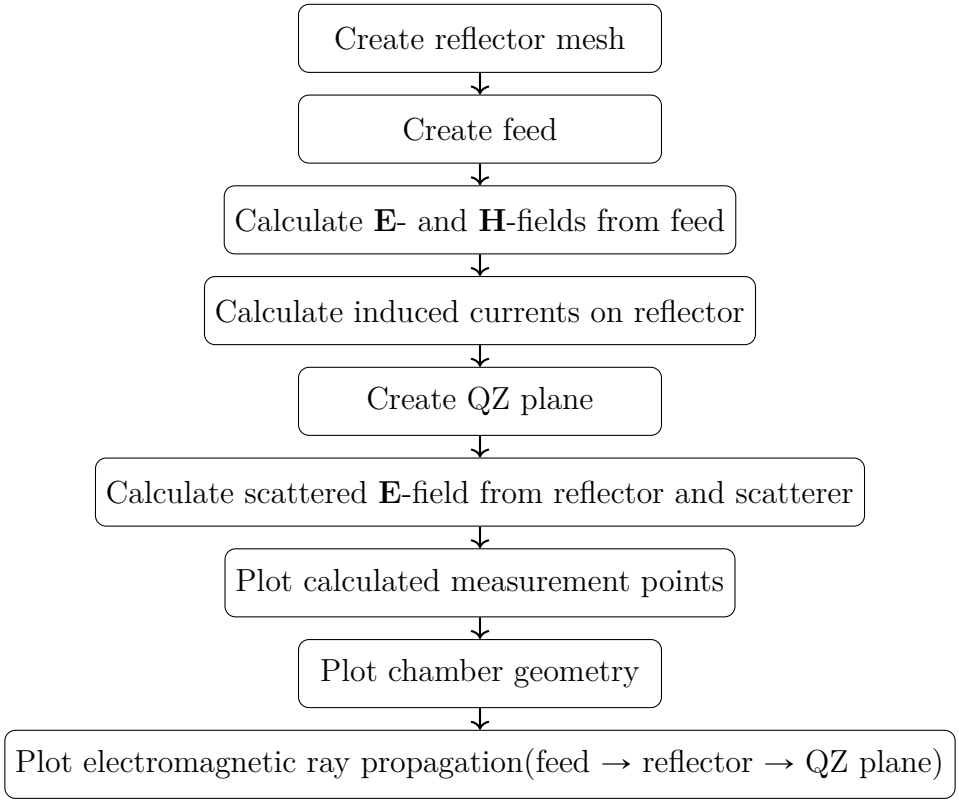

Figure 3.1: System overview of the simulation workflow.

Additionally, exact chamber and reflector dimensions are omitted due to confidentiality. Where possible, dimensions are reported in wavelengths or as relative quantities.

3.1 Reflector Creation

The reflector geometry was generated by first defining the rectangular rim of the reflector in the local xy-plane. The rim dimensions were determined from the reflector datasheet provided by the manufacturer. A set of interior seed points was

then created by placing a Cartesian grid inside the bounding box of the rim. Points located inside the rim boundary were retained using a polygon-inclusion test, while points outside the boundary were discarded.

The rim points and the retained interior points were then used to construct a constrained Delaunay triangulation. The rim edges were included as constraints in order to preserve the outer reflector boundary during the triangulation. After the initial triangulation, triangles located outside the reflector rim were removed by testing the triangle incenters against the rim polygon. This removal procedure is generally only necessary for geometries more complex than a square. The procedure resulted in a cleaned two-dimensional triangular mesh of the reflector aperture, as shown in Fig. 3.2.

The two-dimensional mesh was subsequently mapped onto a parabolic surface using the specified focal distance. This produced the three-dimensional reflector geometry in the local coordinate system. The focal point was defined at a distance equal to the focal length along the local reflector axis, as illustrated in Fig. 3.3.

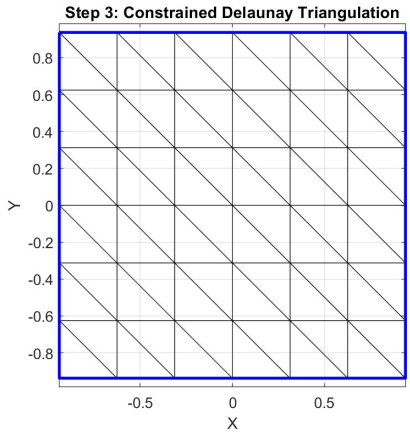

Figure 3.2: Rectangle mesh.

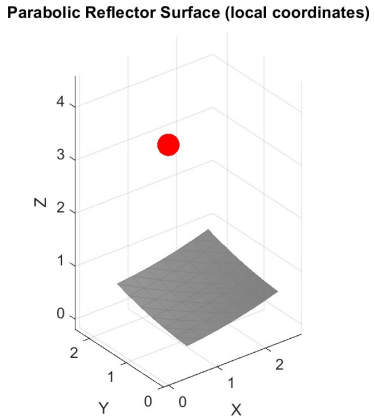

Figure 3.3: Reflector parabolic mesh. Red dot is the focal point

Finally, the reflector surface was transformed from the local coordinate system to the global coordinate system used in the chamber model. This was done by defining a reflector coordinate system with the desired origin and orientation, and then transforming all mesh vertices and the focal point into global coordinates.

The resulting reflector was stored as a triangular surface structure containing the global vertex coordinates, triangle connectivity, operating frequency, and surface type. For each triangular element, the centroid, unit normal vector, and surface area were calculated. These quantities are later used when evaluating the electromagnetic fields and induced surface currents on the reflector.

3.2 Feed Creation

The feed model was developed incrementally, beginning with an idealized infinitesimal electric dipole source and later extended to a discretized aperture representation of a realistic horn antenna.

In the simplest configuration, a single infinitesimal electric dipole source was implemented by defining a point in space together with a current vector representing the aperture current density. The direction of this vector also determines the polarization of the antenna, as illustrated in Fig. 3.4.

To obtain a more realistic antenna representation, the feed aperture was later discretized into a planar square mesh of incremental current sources, as shown in Fig. 3.5. The spacing between adjacent source elements was chosen to be at most $\lambda/4$. This spacing ensures sufficiently dense spatial sampling of the aperture current distribution and helps preserve the validity of the Huygens–Fresnel principle while reducing numerical artifacts such as spatial aliasing and grating lobes.

Each source element in the aperture mesh was assigned the same polarization direction, while the current amplitude distribution across the aperture could be controlled independently. In order to produce a more realistic beam formation, a two-dimensional Gaussian taper was implemented across the aperture, giving the highest amplitude at the center of the feed and gradually decreasing toward the edges, as illustrated in Fig. 3.6. This results in smoother aperture illumination and more realistic radiation characteristics.

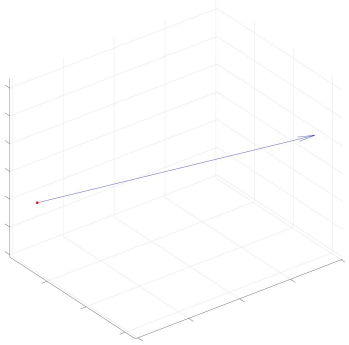

Figure 3.4: Single incremental source.

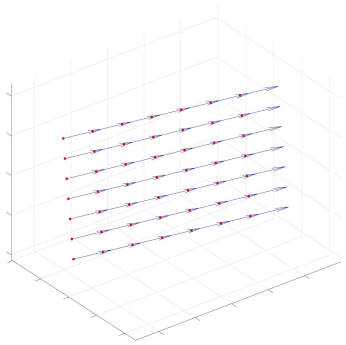

Figure 3.5: Mesh with incremental sources.

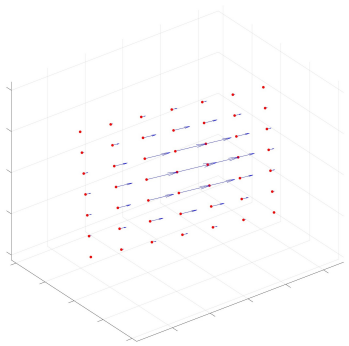

Figure 3.6: Mesh with Gaussian distribution.

The feed was modeled in a dedicated local coordinate system whose origin was placed at the reflector focal point. Separate rotation operations around the local x-, y-, and z-axes were implemented, allowing the feed orientation to be adjusted freely in space. By default, the feed is positioned at the focal point and directed toward the center of the reflector, although finer angular adjustments can be made by the user.

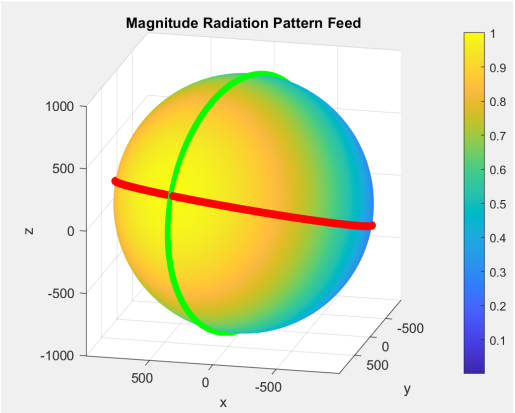

Figure 3.7: Directivity of the implemented Huygens source.

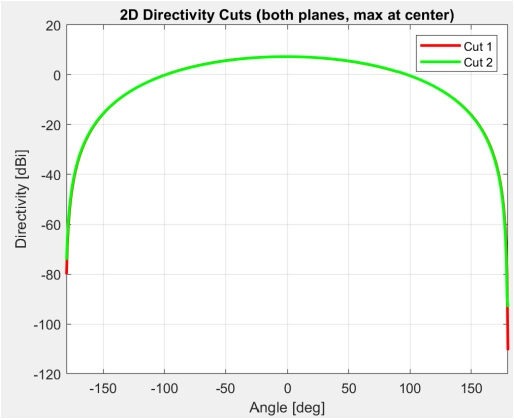

Figure 3.8: Radiation pattern cuts of Huygens source.

At a later stage, the feed model was modified by replacing the electric dipole sources with Huygens sources in the aperture mesh in order to suppress back radiation and obtain more physically realistic radiation characteristics. The Huygens sources in the feed aperture was linearly polarized along the x-direction in the global coordinate system. The resulting radiation pattern and antenna gain were validated via directivity evaluation and radiation cuts. For an individual Huygens source element, a directivity of 4.7 dBi was obtained, as shown in Fig. 3.8, confirming the expected element-level performance.

In addition to the baseline feed configuration, a more directive feed model with approximately 20 dBi directivity was also generated for one of the investigations in Sec. 3.7. The higher-directivity feed was obtained using the same aperture-based Huygens source formulation, with the Gaussian taper across the aperture distribution increased from -1 dB to -50 dB, together with an increased effective aperture size. This produced a narrower main beam and reduced edge illumination on the reflector. The resulting radiation characteristics were verified through inspection of the principal-plane radiation pattern cuts and directivity evaluation.

3.3 Measurement Planes: Quiet Zone and Field Cuts

The QZ was defined as a planar measurement region located in front of the reflector. The plane is positioned at a specified distance from the reflector and is oriented parallel to the reflector aperture. This region is used to evaluate the field distribution in the intended test volume of the chamber.

In addition to the QZ plane, orthogonal field cuts were also generated. These cuts are measurement planes perpendicular to the QZ and are used to study how the field varies along the propagation direction. Together, the QZ and the field cuts provide both transverse and longitudinal information about the field behavior inside the chamber.

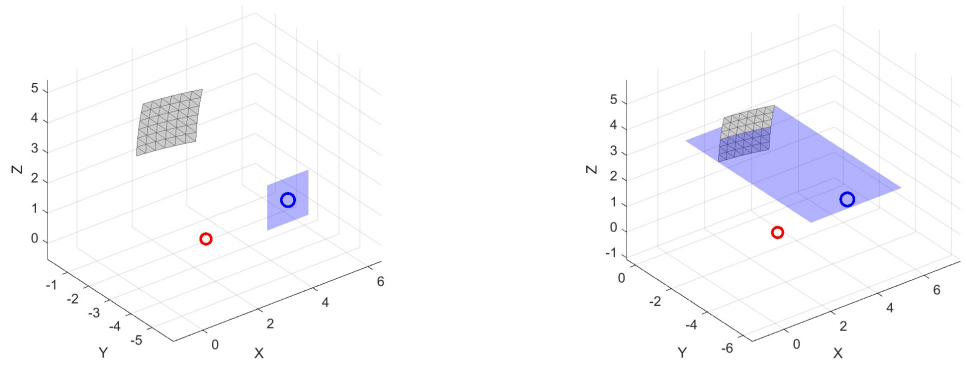

(a) Chamber with QZ. **(b)** Chamber with field cut.

Figure 3.9: Visualization of the measurement regions in the chamber. The red marker indicates the focal point where the feed antenna is positioned, the grey surface represents the reflector, and the blue regions show the measurement points. The blue marker indicates the center of the QZ.

The QZ was generated by defining a center point at the specified distance along the reflector propagation direction, after which a square $N \times N$ grid was constructed in a plane parallel to the reflector aperture.

The field cut was generated in a similar way, but using a plane orthogonal to the QZ. This plane extends from the reflector region toward the QZ and is used to observe the field development along the chamber propagation direction. The cut is therefore useful for visualizing the focusing behavior and the field uniformity before and inside the QZ.

Fig. 3.10 illustrates the global coordinate system together with the local coordinate systems associated with the reflector and feed. The reflector coordinate system defines the aperture orientation and propagation direction toward the QZ.

3.4 Ray Tracing

A ray-tracing routine was implemented to visualize and verify the geometrical path from the feed to the reflector and further toward the QZ. Rays are generated from the feed position to selected triangular elements on the reflector surface. The number of traced rays can be adjusted by selecting all reflector triangles or only a subset of them.

For each selected reflector triangle, the ray is first drawn from the feed position to the triangle centroid. The local surface normal of the triangle is then used to calculate the reflected ray direction according to the law of reflection,

$$\hat{\mathbf{e}}_\mathrm{r} = \hat{\mathbf{e}}_\mathrm{i} - 2\,(\hat{\mathbf{e}}_\mathrm{i} \cdot \hat{\mathbf{n}})\,\hat{\mathbf{n}}, \tag{3.1}$$

where $\hat{\mathbf{e}}_\mathrm{i}$ is the incident ray direction, $\hat{\mathbf{e}}_\mathrm{r}$ is the reflected ray direction, and $\hat{\mathbf{n}}$ is the unit normal vector of a plane.

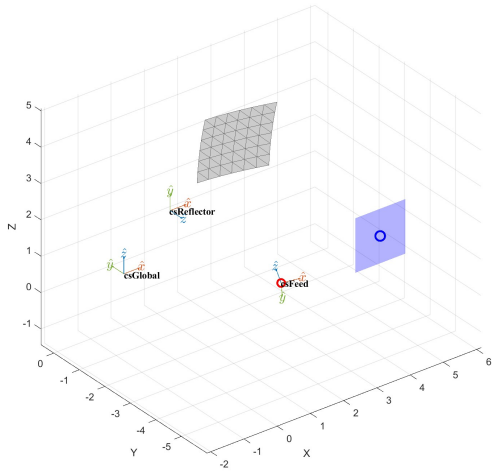

Figure 3.10: Coordinate systems used for the chamber, reflector, and feed.

The intersection between the reflected ray and the QZ plane is then calculated using a line–plane intersection. The intersection parameter is given by

$$t = \frac{\hat{\mathbf{n}} \cdot (\mathbf{P}_p - \mathbf{P}_0)}{\hat{\mathbf{n}} \cdot \mathbf{v}}, \tag{3.2}$$

where $\mathbf{P}_0$ is a point on the line, $\mathbf{v}$ is the line direction vector and $\mathbf{P}_p$ is a point on the plane. The intersection point is then obtained as

$$\mathbf{P} = \mathbf{P}_0 + t\mathbf{v}. \tag{3.3}$$

Combining these expressions gives

$$\mathbf{P} = \mathbf{P}_0 + \left(\frac{\hat{\mathbf{n}} \cdot (\mathbf{P}_p - \mathbf{P}_0)}{\hat{\mathbf{n}} \cdot \mathbf{v}} \right) \mathbf{v}. \tag{3.4}$$

This procedure is repeated for each selected reflector triangle. For every ray, the total propagation distance is calculated as the sum of the distance from the feed to the reflector centroid and the distance from the reflector centroid to the QZ intersection point. This provides a simple verification of the reflector geometry, since a correctly focused parabolic reflector should produce nearly equal optical path lengths from the feed through the reflector to the QZ. The rays are visualized in Fig. 3.11a.

The resulting lengths are illustrated in Fig. 3.11b. The maximum difference between the optical path lengths was 0.006λ, which was attributed to the discretization of the reflector surface, where the centroids of the triangles did not perfectly follow the ideal parabolic geometry.

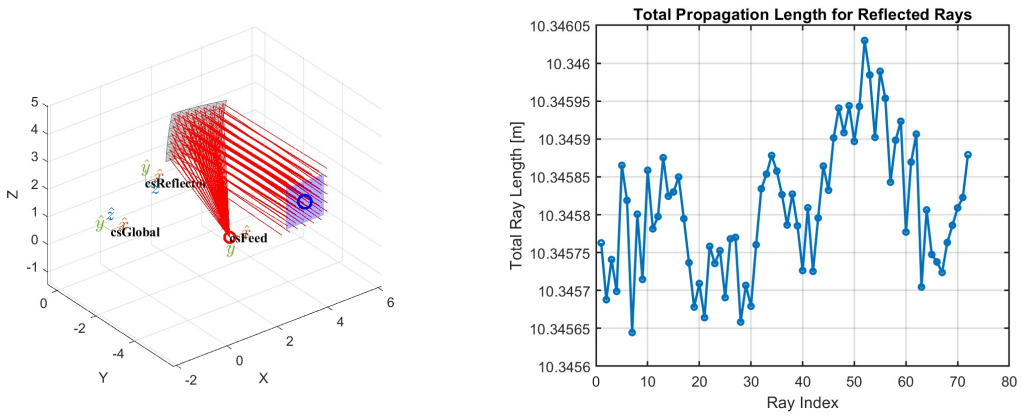

(a) Ray tracing from the feed to the reflector and further to the QZ.

(b) Total propagation length of the traced rays.

Figure 3.11: Ray-tracing verification of the reflector geometry. The traced rays are used to confirm that the total propagation lengths are approximately equal.

3.5 Verification of PO function

An already developed MoM solver was used to validate the implemented PO algorithm. The MoM solver was developed by Rob Maaskant and has previously been verified to be reliable and produce accurate results. Therefore, it was used as a reference solution when evaluating the performance and reliability of the PO implementation.

Due to the fact that the MoM solution becomes computationally expensive for electrically large structures, the first validation was performed using the $5\lambda \times 5\lambda$ flat reflector at 4 GHz.

The initial validation case used a Hertzian dipole illuminating the plate. The dipole was positioned along the center of the plate such that the plate was symmetrically illuminated. The simulations were performed with the dipole located at the following distances from the plate: 2λ, 5λ, 7.5λ, and 10λ. These tests were conducted to evaluate the performance of the PO method for a plate illuminated by sources positioned at varying distances and consequently producing incident fields with different curvature. In addition, the agreement between the PO and MoM solutions is assessed as the source distance increases and the incident field progressively approaches a plane-wave approximation.

A second scenario was observed and it used a scaled reflector setup. This scenario was geometrically scaled to maintain proportional relationship between the reflector, feed and QZ to ensure that the electromagnetic behavior remains representative of a full-scale chamber. The parabolic reflector featured an aperture size of $10\lambda \times 10\lambda$ and was illuminated by a dipole feed source. This specific electrical size was chosen because it represented the upper bound of the computational capacity of the simulation hardware, a larger geometry exceeded the available laptop memory for a full-wave MoM solution. For this particular setup, a corresponding linear system

contained 36080 unknowns.

Several performance metrics were used to evaluate the agreement between the PO and MoM surface current results for both the plate and the reflector configurations. The following metric were used to evaluate the PO function: surface current density magnitude $|\mathbf{J}_s|$ was evaluated across the plate surface to assess how well the current from PO matches the MoM reference. The relative surface current error, accounting for both magnitude and phase, was computed per triangle normalized locally by the triangle's own current magnitude as

$$e_{\text{tri},i} = \frac{|J_{s,i}^{\text{PO}} - J_{s,i}^{\text{MoM}}|}{|J_{s,i}^{\text{MoM}}|} \tag{3.5}$$

and the relative global current was calculated and normalized by the peak surface current as

$$e_{global,i} = \left[\frac{|J_{s,i}^{\text{PO}} - J_{s,i}^{\text{MoM}}|}{|J_{s,i}^{\text{MoM}}|_{\max}} \right] \tag{3.6}$$

where $i = 1, ..., N_t$ denotes the mesh triangle index and $J_{s,i}$ is the surface current density evaluated at the centroid of the i-th triangle. The same centroid locations were used for both the PO and MoM solutions. The RMS and mean values of the error measures were computed over all mesh elements and are denoted as RMS(e_{tri}), Mean(e_{tri}), RMS(e_{global}), and Mean(e_{global}), where e_{tri} and e_{global} represent the set of all element-wise errors $e_{\text{tri},i}$ and $e_{\text{global},i}$ respectively.

The similarity between the complex surface current vectors obtained from the PO and MoM methods was evaluated using the normalized Hermitian inner product (cosine similarity)

$$S_C = \frac{\overline{(\mathbf{J}_s^{\text{PO}})}\mathbf{J}_s^{\text{MoM}}}{\|\mathbf{J}_s^{\text{PO}}\| \, \|\mathbf{J}_s^{\text{MoM}}\|} \tag{3.7}$$

where $\overline{(\cdot)}$ denotes the conjugate and the reported similarity is obtained by averaging S_C, denoted by $S_{C,\text{avg}}$.

3.6 Constructing The Scattering Plate

The scattering object was modeled as a two-dimensional surface based on parameters such as width, length and mesh resolution. The scattering object was defined with its own local coordinate system, where the normal surface was oriented along the $+\hat{z}$-axis direction. The surface was assumed to be a infinitesimal thin plate PEC. This provided a simplified first-order representation of the scattering behavior toward the QZ. Material losses, coatings, and other structural details were neglected.

For visualization purposes, a coarser representation of the mesh is shown in Fig. 3.12, whereas the simulations were performed using a finer mesh of $\lambda/10$. Furthermore, the local coordinate system was employed to facilitate object transformations, such as

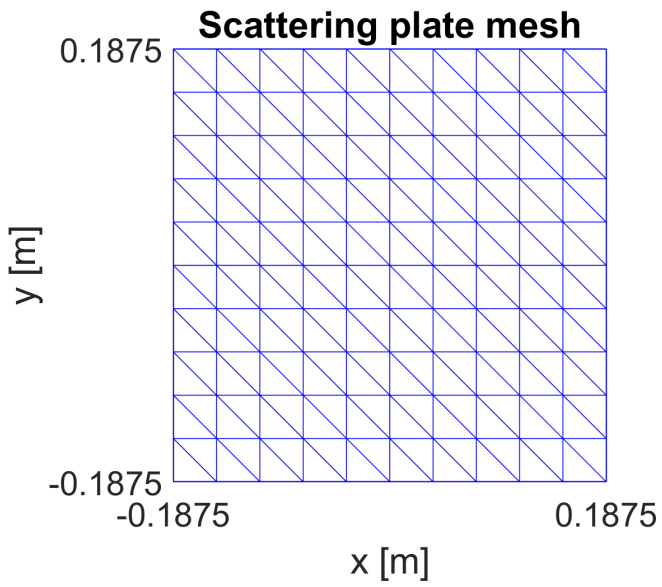

Figure 3.12: A $5\lambda \times 5\lambda$ scattering plate at 4 GHz, shown with a coarse mesh resolution of $\lambda/2$ for visualization purposes.

rotations making it independent of the global coordinate system. Fig. 3.13 illustrates the local coordinate system together with the scattering plate.

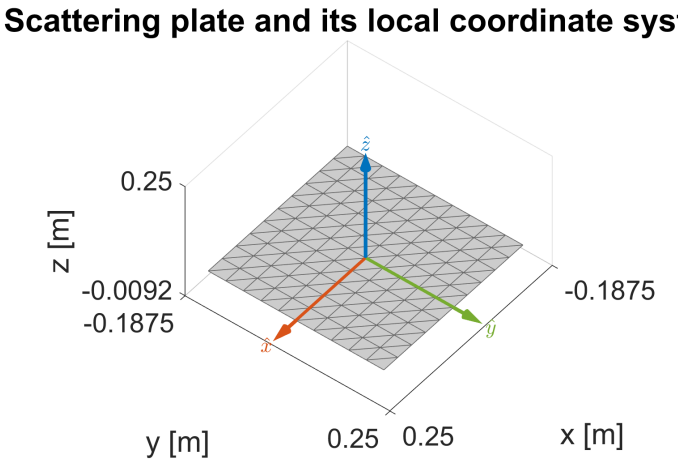

Figure 3.13: Scattering plate and the local coordinate system used to rotate the plate

For each instance of the scattering object, the geometric information required for MoM was stored, including surface vertices, triangular mesh elements, centroids and normal vectors of each triangle element. The normal vectors and centroids of each triangle patch are illustrated in Fig. 3.14.

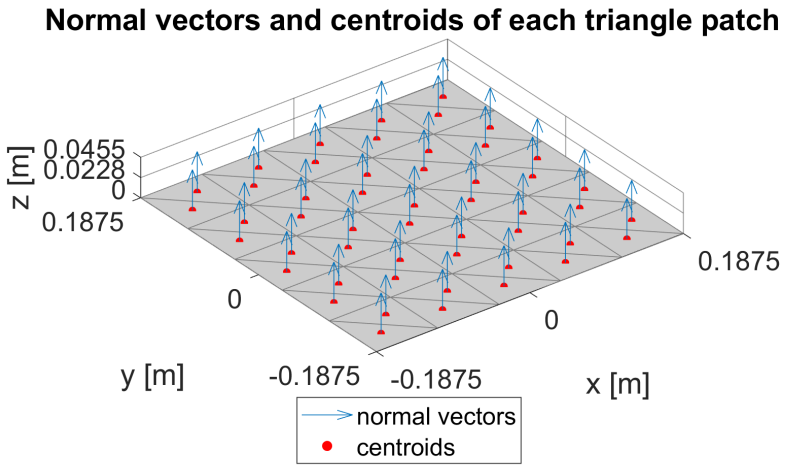

Figure 3.14: Coarse discretization of the scattering plate to illustrate the calculation of triangle patch centroids and normal vectors

3.7 QZ Metrics Validation

To evaluate the simulation framework and the behavior of the QZ metrics under different configurations, a set of six cases was defined. The cases were designed to isolate the effects of reflector size, edge treatment, and aperture illumination. The results are analyzed comparatively, with focus placed on identifying physically consistent trends in quiet zone uniformity across the different configurations. All simulations were performed at 4 GHz using an offset reflector configuration.

1. The first case considered an offset reflector without serrated edges. This case serves as the reference configuration for evaluating the effect of serrations on the QZ performance.

2. The second case consists of an offset reflector with serrated edges applied along the reflector boundary, used to investigate edge diffraction effects.

3. The third case employed an offset reflector with serrated edges together with a modified feed illumination to achieve a more uniform aperture illumination across the reflector surface. This configuration was used to study the influence of reduced edge illumination.

4. The fourth case introduced a larger reflector geometry together with serrated edges. The purpose of this configuration was to study the influence of reflector scaling on QZ performance while maintaining identical excitation conditions.

5. The fifth case employed a strongly tapered feed radiation pattern in order to reduce the illumination near the reflector edges. This configuration was used to analyze the influence of edge illumination on diffraction effects.

6. In the sixth and final case, a scattering plate was introduced into the cham-

ber environment. This configuration was used to investigate the influence of additional scattering mechanisms on the QZ performance.

In the sixth case, the scattering plate was positioned at (1.3800, 0, 3.3000) m in the global coordinate system. Its orientation was defined such that the surface normal lies in the plane spanned by the vectors from the feed to the plate center and from the plate center to the QZ center. The orientation was implemented using successive rotations of 105.6536° about x, 8.1300° about y, and 10.7081° about z. This is displayed in Fig. 3.15.

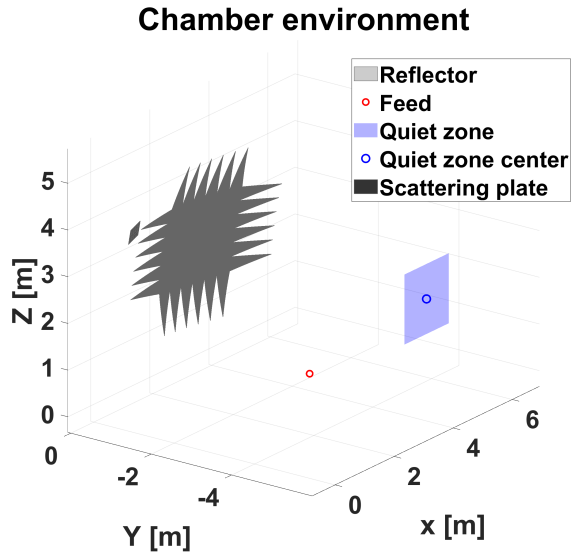

Figure 3.15: Chamber setup with scattering plate introduced.

The plate was illuminated by the direct field from the feed. Second-order and multiple reflections between the plate and reflector were neglected due to their expected negligible contribution within the chamber.

Table 3.1 provides a summary of each case. Nominal reflector size refers to the baseline reflector geometry defined in the physical chamber design. Additionally, Center-directed illumination refers to a feed configuration aimed toward the reflector center, resulting in a non-evenly aperture field due to the offset reflector geometry.

The electric field magnitude over the QZ was evaluated using the mean value, root-mean-square (RMS), peak-to-peak variation, and standard deviation. In addition, the XPD was computed to quantify the polarization purity of the field distribution. The polarization tilt angle between the E_x and E_z field components was evaluated at the QZ center to characterize the polarization orientation.

The root-mean-square (RMS) value of the co-polarized electric field magnitude is computed as

$$E_{co,\mathrm{RMS}} = \sqrt{\frac{1}{N}\sum_{k=1}^{N} |E_{\mathrm{co},k}|^2}. \tag{3.8}$$

Table 3.1: Overview of simulation cases used for QZ metric validation. All cases use an offset reflector operating at 4 GHz.

Case	Reflector size	Serrations	Feed illumination	Plate	Solver
1	Nominal	No	Center-directed illumination	No	PO
2	Nominal	Yes	Center-directed illumination	No	PO
3	Nominal	Yes	symmetric aperture illumination	No	PO
4	Large	Yes	Center-directed illumination	No	PO
5	Nominal	No	Strongly tapered illumination	No	PO
6	Nominal	Yes	Center-directed illumination	Yes	PO & MoM

where $E_{\mathrm{co},k}$ denotes the co-polarized component of the eletric field evaluated at sample point k and N is the total number of sampling points.

For consistency with other reported magnitude metrics, the RMS value is additionally expressed in decibels as a post-processing step using $20\log_{10}(\cdot)$. In the reported results, RMS values are presented in both linear and dB scale.

The XPD is evaluated pointwise as the ratio between co-polar and cross-polar field components in dB. The reported XPD value correspond to the worst case value within the evaluated QZ region.

The phase of the co-polarized electric field component is computed from the complex field as $\angle(E_{\mathrm{co}})$ and subsequently unwrapped to remove 2π discontinuities. The unwrapped phase is then referenced to the center of the QZ, such that the phase at the QZ center is set to zero degrees.

All phase-based statistics (mean, RMS, peak-to-peak variation, and standard deviation) are computed on this unwrapped and center-referenced phase distribution. This ensures that phase metrics represent spatial phase variations within the QZ and are not affected by discontinuities introduced by phase wrapping.

4

Results

This section presents the results obtained from the CATR model, including the characterization of the feed model, validation of the PO implementation and the evaluation of the QZ performance.

4.1 Feed

The aperture feed model's radiation pattern is presented in Fig. 4.1, normalized to its maximum value. This pattern illustrates the overall directivity of the feed antenna, showing a main lobe and reduced radiation in the back-side region.

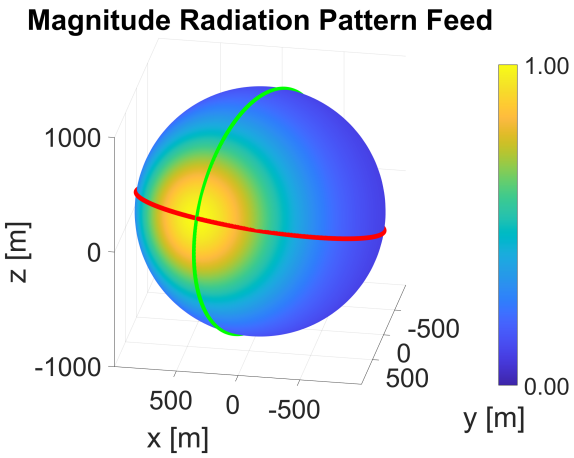

Figure 4.1: Radiation pattern of the aperture feed model.

Fig. 4.2 displays the cuts of the radiation pattern, where Cut 1 represents the horizontal cut. Meanwhile, Cut 2 represents vertical cut. The feed has a directivity of 10.6 dBi. Both plane cuts show a stable main beam with relatively symmetric roll off characteristics.

The final comparison in Fig. 4.3 shows the reference radiation patterns provided in the antenna datasheet along with the simulated aperture feed model. It can be observed that the aperture model follows the reference pattern closely up to approximately 50 degrees off-boresight, beyond which deviations become more pronounced. This level of agreement is considered acceptable for the CATR analysis as the region beyond 50 degrees contributes minimally to the reflector illumination.

Furthermore, the reflector in the CATR configuration is illuminated under a subtended angle of approximately 17 degrees from the feed position. To evaluate the agreement between the simulated feed model and the desired illumination characteristics, quantitative deviation metrics, including the maximum deviation and RMS deviation within $\pm 17^{\circ}$ were computed. The results are presented in Table 4.1. In this region, the simulated aperture model aligns well with the reference pattern, indicating that the model accurately captures the dominant part of the radiation

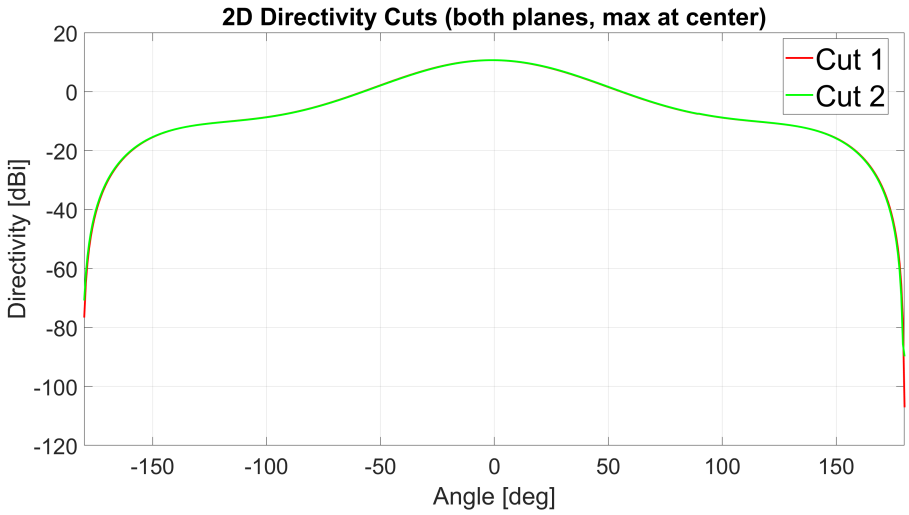

Figure 4.2: Horizontal and vertical cut of the feed radiation pattern.

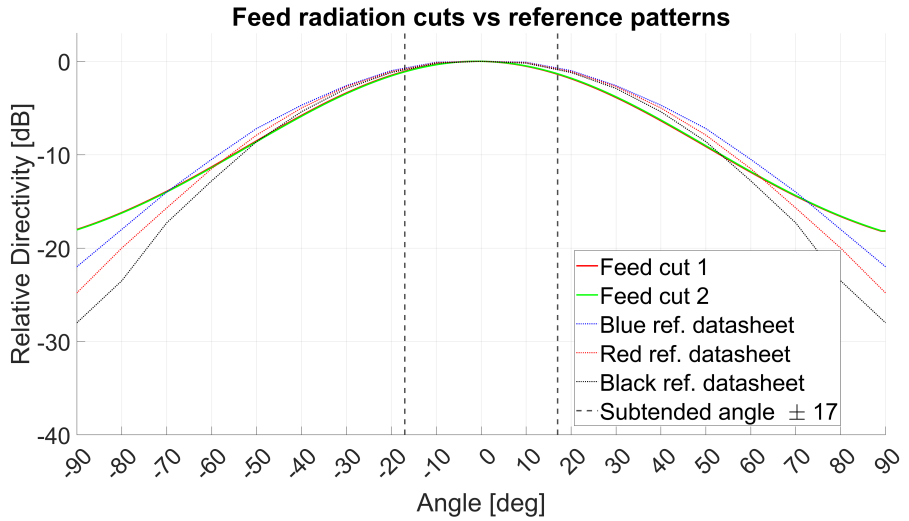

Figure 4.3: Feed cuts vs reference patterns from datasheet of physical feed antenna

Table 4.1: Deviation between the simulated feed radiation cuts and the reference feed taper curves within $\pm 17^\circ$ from boresight.

Feed cut	Maximum deviation (dB)	RMS deviation (dB)
Cut 1	1.373	0.496
Cut 2	1.320	0.491

pattern within the region of interest. The maximum deviations are approximately 1.3 dB, with RMS deviations of approximately 0.5 dB. The low RMS deviation confirms that the aperture feed model reproduces the reference illumination taper accurately across the reflector surface. These deviations are considered acceptable for the intended reflector illumination within the $\pm 17^\circ$ range.

4.2 Verification of PO

This section describes the results of the validation of the PO method.

4.2.1 Square Reflector

Fig. 4.4 displays the setup to validate the PO function, 4 GHz at four different feed distances illuminating a $5\lambda \times 5\lambda$ flat reflector.

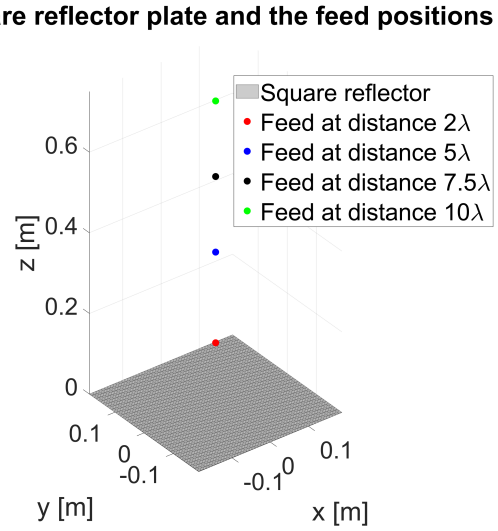

Figure 4.4: Setup of the square reflector plate and different feed positions across $2\lambda - 10\lambda$.

Fig. 4.5 illustrates the magnitude current, $|\mathbf{J}_s|$ and the relative error, e_{global}, between the PO and MoM solutions evaluated per triangle on the square plate in linear scale. It can be observed that the PO approximation agrees well with the MoM solution in the interior region of the plate, where the induced currents vary smoothly. The visualization further highlights the regions where the PO approximation begins to deviate from the MoM reference solution, particularly near the plate edges where the diffraction effects neglected by PO become more pronounced.

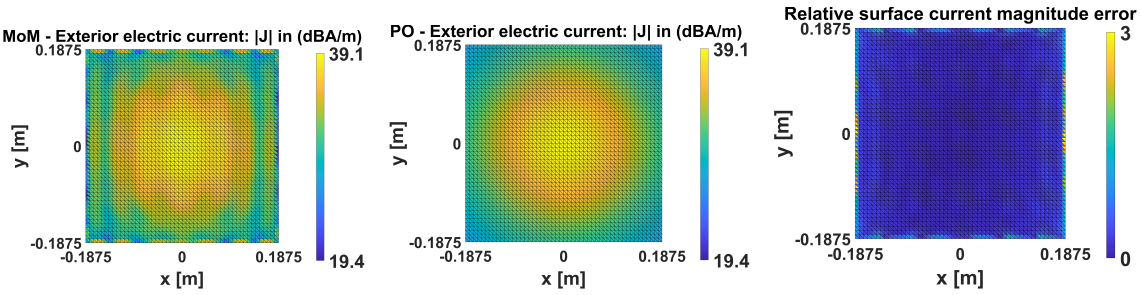

(a) MoM surface current magnitude. **(b)** PO surface current magnitude. **(c)** Relative error e_{global}.

Figure 4.5: Magnitude current on the $5\lambda \times 5\lambda$ square plate reflector: MoM, PO, and their difference at feed distance 2λ distance.

Fig. 4.6 shows the surface current magnitude for both MoM and PO at a feed distance of 5λ. Compared to the 2λ case, the MoM solution show an oscillatory pattern across the plate. This effect is caused by the phase variation of the incident field over the finite plate and by the mutual coupling between the surface current basis functions, which leads to interference effects that are captured by MoM. In contrast, the PO solution appears smoother and more uniform, with a slight increase in magnitude toward the center of the plate. This is because PO assumes a locally

plane wave approximation and neglects interactions between different parts of the surface and therefore cannot capture the same accuracy as MoM.

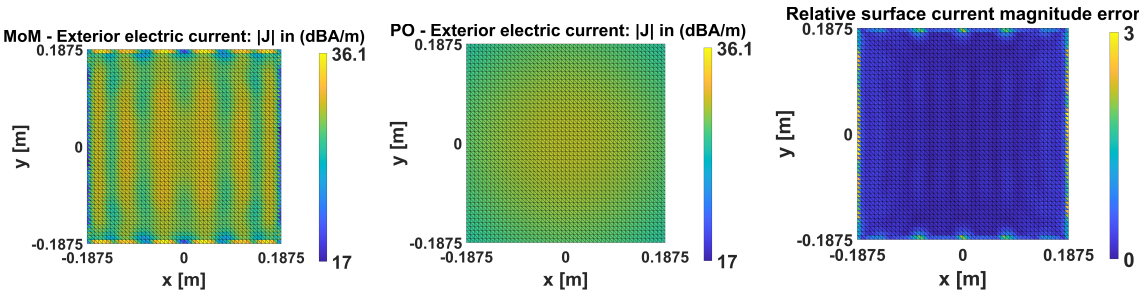

(a) MoM surface current magnitude. **(b)** PO surface current magnitude. **(c)** Relative error e_{global}.

Figure 4.6: Surface current magnitude distributions on the $5\lambda \times 5\lambda$ square plate reflector computed using MoM and PO, together with their relative difference for a feed distance of 5λ.

Fig. 4.7 display the surface current magnitude of MoM, PO and the relative difference at a feed distance of 7.5λ. The incident field increases to resemble a plane wave, reducing the phase variations across the plate and the interference effects captured by MoM become weaker. Meanwhile, the PO current magnitude have become closer to uniform distribution across the plate. However, the largest error remain at the edges of the plate. Lastly, at feed distance of 10λ, the oscillatory pattern observed in

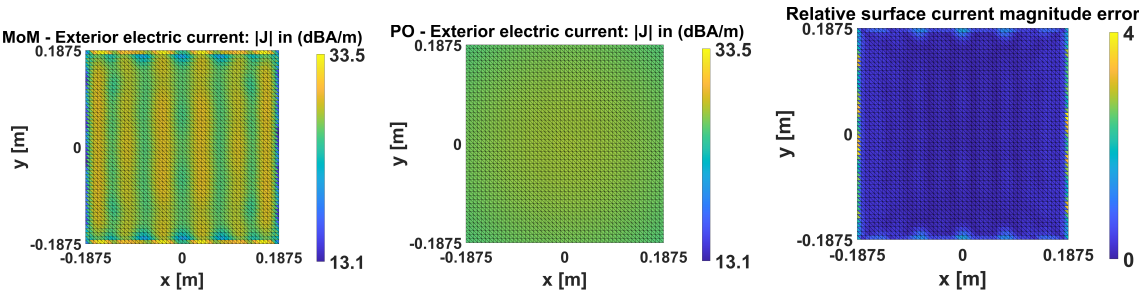

(a) MoM surface current magnitude. **(b)** PO surface current magnitude. **(c)** Relative error e_{global}.

Figure 4.7: Magnitude current on the $5\lambda \times 5\lambda$ square plate reflector: MoM, PO, and their difference at feed distance 7.5λ distance.

the MoM current in Fig. 4.8 is still present but with reduced magnitude and similar contrast. This reflects the more uniform illumination of the plate as the incident field approaches a plane wave. Meanwhile, PO is more uniform across the plate. The deviations between the two methods remain near the edges, where diffraction is not captured by PO.

The validation results of the PO implementation compared to the MoM solution are presented in Table 4.2. The evaluated metrics include the relative RMS error and the mean error for $e_{\text{tri},i}$ (see (3.5)), $e_{\text{global},i}$ (see (3.6)), and S_C (see (3.7)), for different distances between the feed and the plate.

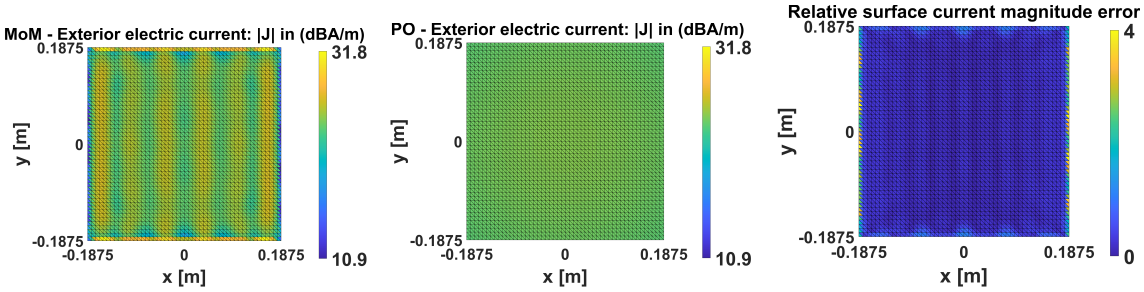

(a) MoM surface current magnitude. **(b)** PO surface current magnitude. **(c)** Relative error e_{global}.

Figure 4.8: Magnitude current on the $5\lambda \times 5\lambda$ square plate reflector: MoM, PO, and their difference at feed distance 10λ distance

It is observed that the similarity metric $S_{C,\text{avg}}$ remains consistently high across all feed distances, indicating that the PO formulation correctly reproduces the dominant current directions on the reflector surface.

However, both the mean and RMS error metrics show a gradual increase with increasing feed distance. This trend should be interpreted with care. Since the field is normalized by the peak current magnitude, the error metrics are governed not solely by absolute current levels but also by the relative distribution of energy over the reflector surface.

At larger feed distances, the illumination becomes more uniform across the reflector aperture, which increases the relative contribution of edge regions. In these regions, PO and MoM are known to differ more significantly due to diffraction and edge interaction effects not fully captured by PO. Consequently, the overall RMS error increases even though the central region agreement remains high. Additionally, the observed 15% RMS error is attributed to the relatively small size of the $5\lambda \times 5\lambda$ plate, for which PO begins to lose accuracy.

Therefore, the observed trend is primarily attributed to a combination of normalization effects and the increasing influence of edge-related discrepancies, rather than a simple reduction in induced current magnitude.

Distance (λ)	**RMS**(e_{tri})	**Mean**(e_{tri})	**RMS**(e_{global})	**Mean**(e_{global})	$S_{C,\textbf{avg}}$
2	0.35	0.21	0.1168	0.092	0.9876
5	0.41	0.24	0.1456	0.1097	0.9901
7.5	0.44	0.26	0.1526	0.1152	0.9918
10	0.47	0.27	0.150	0.1136	0.9927

Table 4.2: Comparison of PO and MoM relative RMS error (per triangle and global) and alignment for different feed distances.

4.2.2 Parabolic Reflector

Fig. 4.9 illustrates the parabolic reflector setup used for the comparison between the PO and MoM methods with the focal distance being 23.3λ from the reflector.

Fig. 4.10 presents the surface current magnitude obtained using both methods, together with the global relative error $e_{\text{global},i}$(linear scale) defined in (3.6).

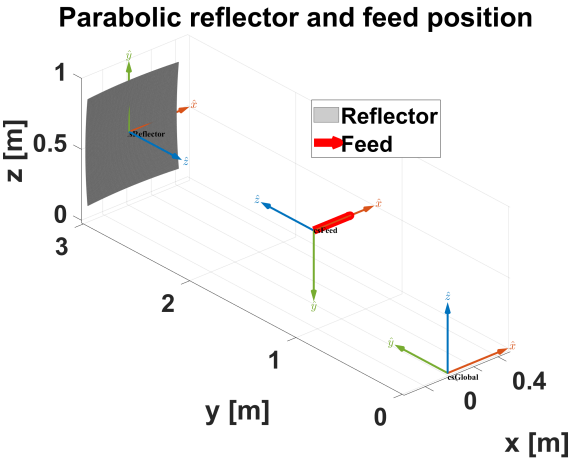

Figure 4.9: $10\lambda \times 10\lambda$ parabolic reflector with the feed located at the focal point.

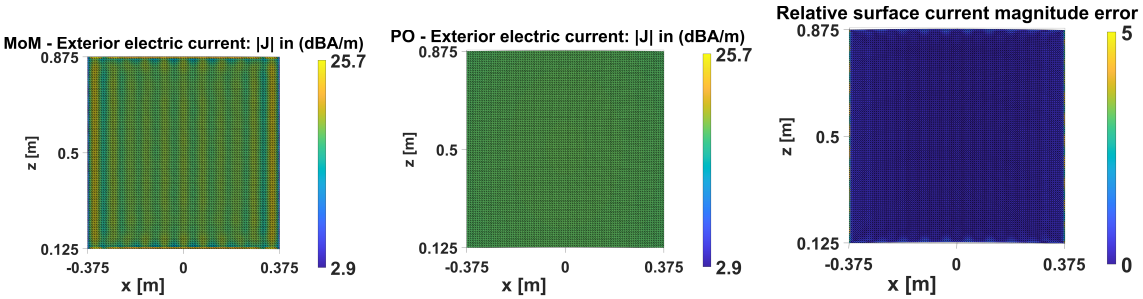

(a) MoM surface current magnitude. **(b)** PO surface current magnitude. **(c)** Relative error e_{global}.

Figure 4.10: Surface current magnitude on the $10\lambda \times 10\lambda$ parabolic reflector obtained using MoM and PO, together with the relative global error between the methods.

The global RMS and mean errors, e_{global}, show only minor differences between the PO and MoM solutions, indicating good overall agreement between the two methods. However, the RMS and mean of the local errors, e_{tri}, is noticeably higher. This further highlights that most variations are caused by the illumination near the reflector edges, where edge triangles are more sensitive and therefore contribute larger local errors. The validation results for the $10\lambda \times 10\lambda$ parabolic reflector are summarized in Table 4.3.

Table 4.3: Comparison between PO and MoM for a $10\lambda \times 10\lambda$ parabolic reflector using different error metrics.

Reflector size	**RMS**(e_{tri})	**Mean**(e_{tri})	**RMS**(e_{global})	**Mean**(e_{global})	$S_{C,\textbf{avg}}$
$10\lambda \times 10\lambda$	0.39	0.21	0.10	0.077	0.99

The results indicate that the PO solution provides a close approximation to the MoM solution for the parabolic reflector case. In particular, the low global error metrics and high cosine alignment confirm that the overall surface current distribu-

tion is accurately captured, while the larger local errors are mainly confined to edge regions.

4.3 Comparison of Chamber configurations and QZ performance

The results of the test cases described in Sec. 3.7 are presented in this section.

The two different base-line chamber environment setups are displayed in Fig. 4.11.

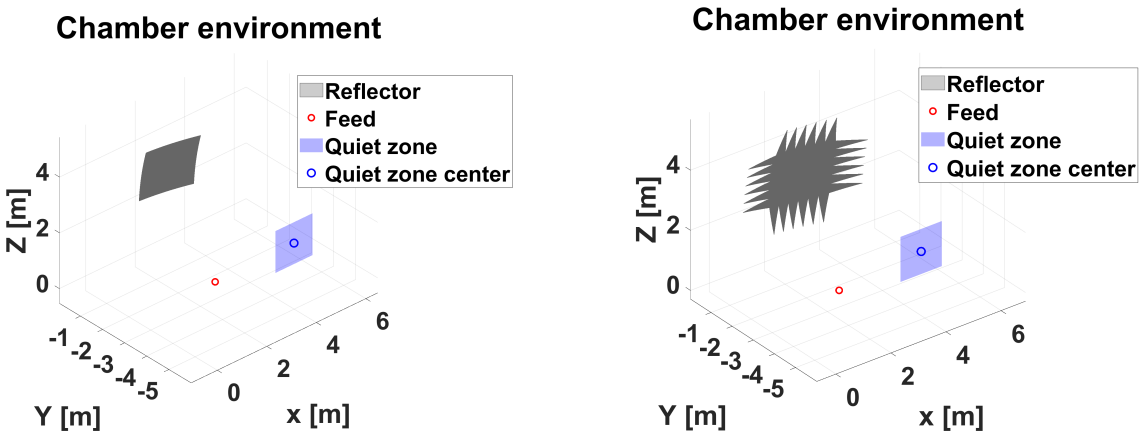

(a) Non-serrated reflector in the chamber setup

(b) Serrated reflector in the chamber setup

Figure 4.11: Comparison of reflector configurations in the chamber setup

There are three test cases based on the baseline chamber configuration shown in Fig. 4.11b: larger reflector, symmetric illumination, and scattering plate configurations. In the alternative chamber configuration shown in Fig. 4.11a, the directive feed setup is evaluated using this chamber configuration.

4.3.1 Test Cases

The horizontal and vertical magnitude cuts for the five cases, normalized by their respective QZ center values are illustrated in Fig. 4.12, where X position indicates the horizontal cut and Z position indicates the vertical cut through the center of the QZ. A clear reduction in the total magnitude variation can be observed when serrated edges are employed, particularly in combination with the increased reflector size, compared to the configuration without serrated edges. The RMS of the magnitude decreases from 0.18 in case 1 to 0.045 in the other two cases, indicating a substantial improvement in the QZ field uniformity.

The even-illumination case demonstrate a lower XPD of approximately 18 dB, around 5 dB lower than the remaining cases. A likely interpretation is that the more uniform reflector illumination increases the excitation of all reflector edges, thereby enhancing edge contributions and cross-polarized field components.

Furthermore, the tapered feed antenna with a gain of 20 dBi exhibits a significantly smaller QZ region, about 0.29 m horizontally and 0.27 m vertically, in Table C.4 in Appendix Chapter C, compared to the other configurations.

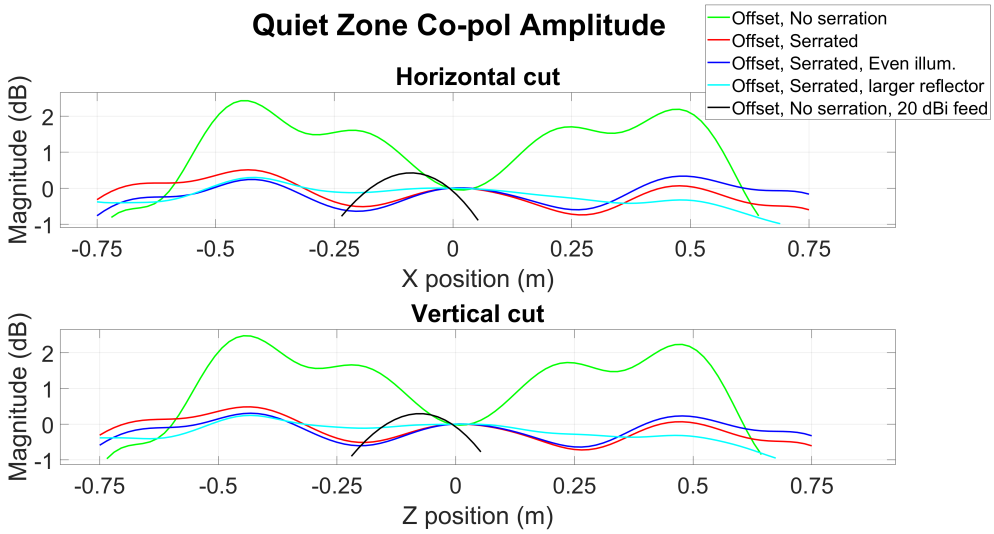

Figure 4.12: Horizontal and vertical magnitude cuts for the five simulation cases, normalized by their respective QZ center values, excluding the scattering-plate case (treated separately in Sec. 4.3.2).

Fig. 4.13 illustrates the phase distribution across the QZ for the five investigated cases. The non-serrated reflector exhibits the largest phase variation across the QZ in both the horizontal and vertical directions. In contrast, the larger serrated reflector provides the smallest phase variation, while the amplitude variation remains close to but partly above 1 dB level. When inspecting the phase in the same case, it varies by a total peak-to-peak variation of 3.89°, both the amplitude and phase are close the standards described in Sec. 2.1.2.1.

Furthermore, the cases with even and non-even illumination exhibit similar phase distributions and overall phase variation characteristics. The larger serrated reflector case exhibits the best performance qualitatively, with both the magnitude and phase variations varying minimally across the QZ. The detailed table evaluation of the QZ characteristics for these cases are described in Appendix C.

4.3.2 Plate Assessment

The sixth and final case is compared to the second case, that is, the offset serrated reflector setup. The setup is based on the chamber geometry shown in Fig. 4.11b, with the addition of a scattering plate positioned beside the reflector. The scattering plate has dimensions of $5\lambda \times 5\lambda$. The corresponding geometrical configuration is illustrated in Fig. 4.14. The scattering plate is illuminated at an angle of approximately 23° relative to the feed antenna pattern, which lies well within the region where the antenna radiation pattern is accurately represented by the radiation pattern from the antenna datasheet as shown in Fig. 4.3.

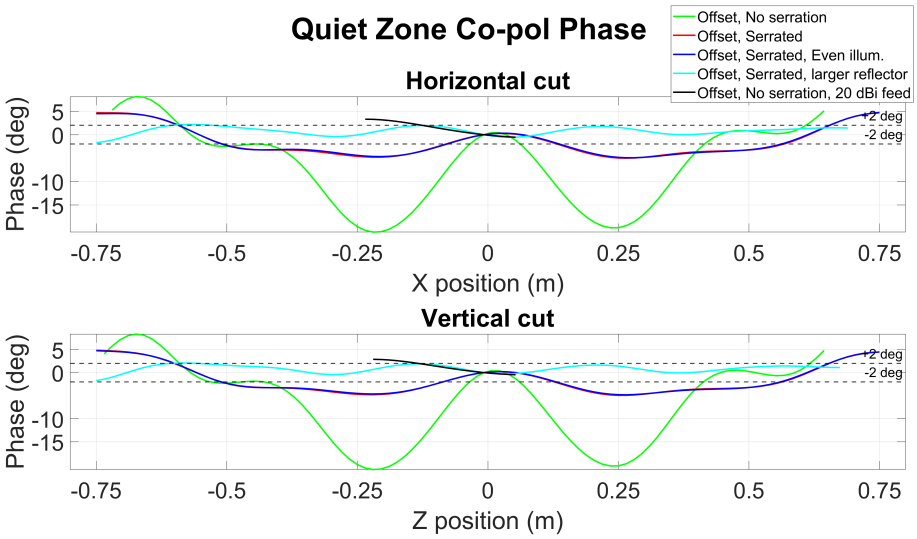

Figure 4.13: Phase cuts across the QZ for the five test cases.

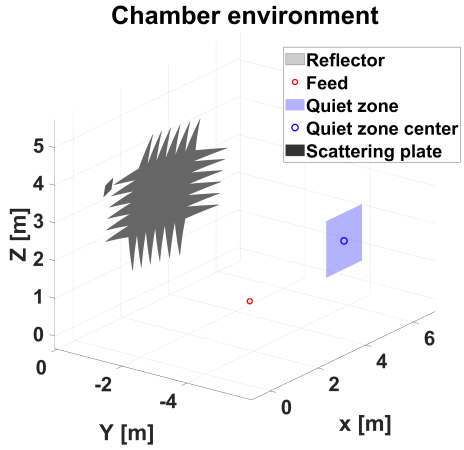

Figure 4.14: Plate introduced in the chamber setup.

The co-polarized component, E_x , in the QZ is shown for two different configurations in Fig. 4.15.

First with only the reflector present in the chamber and second with the scattering plate introduced. Both field distributions are normalized to the maximum field magnitude obtained in the reflector-only case. It can be observed that the presence of the scattering plate significantly alters the field distribution within the QZ, introducing lateral ripple components of 1 dB stronger than the field from the reflector.

Fig. 4.16 presents the co-polarization amplitude along the horizontal and vertical cuts through the QZ center, both normalized to their respective center values.

The serrated reflector produces a peak-to-peak variation of 1.24 dB horizontally and 1.21 dB vertically, remaining close to a 1 dB uniformity level. The introduction of the scattering plate noticeably degrades the amplitude uniformity, increasing the horizontal peak-to-peak variation to 2.71 dB and vertical to 1.77 dB. The RMS

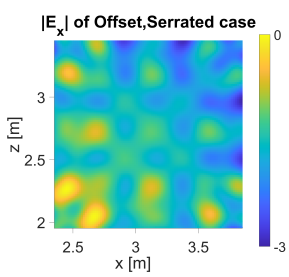

(a) E_{co} across the QZ without the scattering plate.

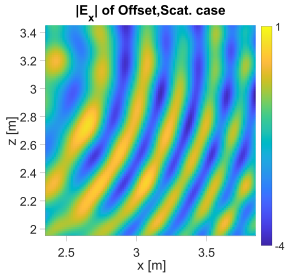

(b) E_{co} across the QZ with the scattering plate

Figure 4.15: Comparison of the co-polarized electric field distribution in the QZ for two configurations: reflector-only and reflector with scattering plate.

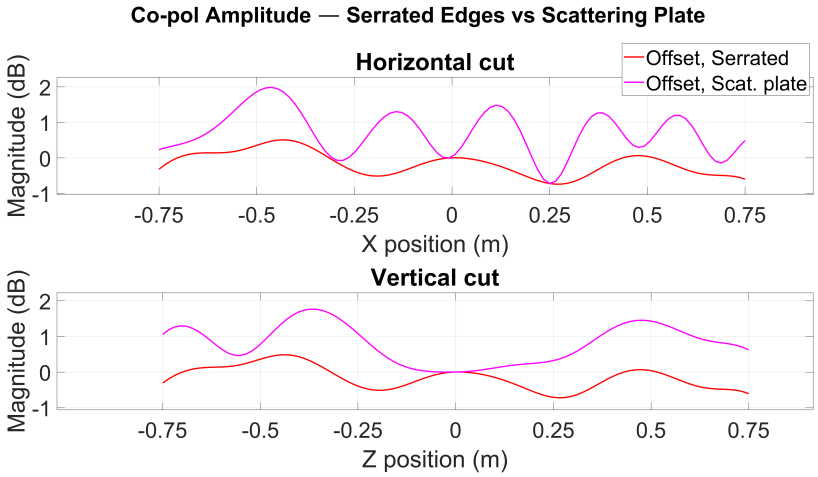

Figure 4.16: Magnitude across the QZ and the magnitude difference.

deviation similarly increases from 0.04 to 0.12 and the standard deviation increases from 0.33 dB to 0.62 dB horizontally.

To quantify the relative strength of the plate's scattered field, Fig. 4.17 presents both total field distributions normalized to the center value of the serrated field, together with the complex difference $|E_{\text{co, serr}} - E_{\text{co, serr+plate}}|$.

The plate contribution lies approximately 15–18 dB below the main reflected field. However, even a field at this level can produce noticeable ripple due to interference with the dominant field, where constructive and destructive interference causes the resulting amplitude to vary. This is consistent with the observed ripple levels in Fig. 4.16.

It can be noted that the ripple from the plate varies across the horizontal cut in Fig. 4.17. As the incidence angle increases from left to right, the ripple period decreases, which is expected and consistent with (2.2). This variation in ripple period is more evident in the horizontal cut than the vertical, as the scattering plate is positioned with a larger lateral offset from the chamber axis in the horizontal plane, resulting in a greater angular variation of the incident scattered field across the hori-

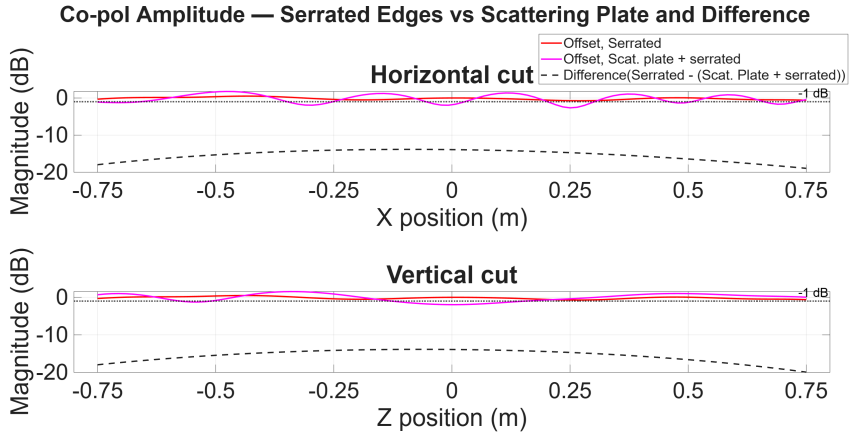

Figure 4.17: Magnitude cuts normalized to same reference and the scattered field contribution from the plate.

zontal side of the QZ. The ripple periods were estimated from the spatial separation between adjacent field maxima in the QZ magnitude distribution. A summary of the left, center and right side ripple periods is displayed in Table 4.4.

Table 4.4: Ripple period across the QZ.

Region	T_{ripple} (λ)
Left Side Ripple	5λ
Center Ripple	3.6λ
Right side Ripple	3.3λ

The corresponding phase distributions and differences are shown in Fig. 4.18. The serrated reflector maintains a peak-to-peak variation of 9.71° horizontally and 9.78° vertically, with an RMS of 3.37° and 3.34° respectively.

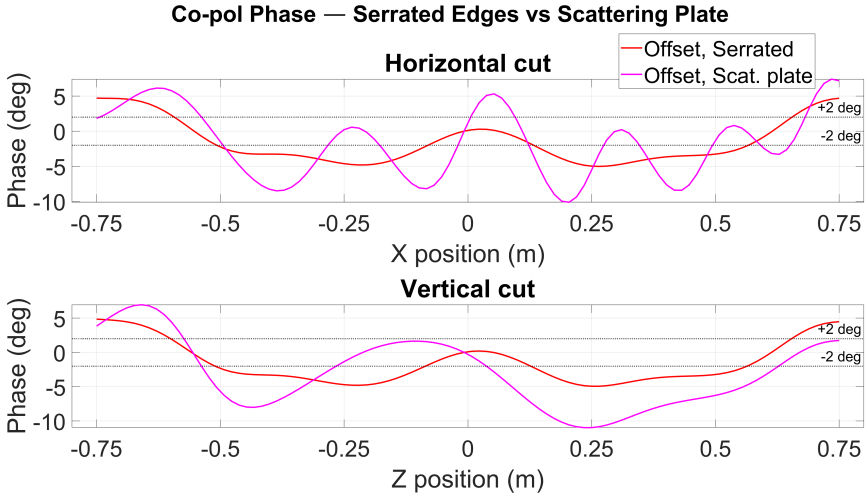

Figure 4.18: Phase across the QZ region and the phase difference between the two cases.

The addition of the scattering plate nearly doubles the phase degradation, with the peak-to-peak variation increasing to 17.51° horizontally and 17.91° vertically and RMS rising to 5.09° and 5.83°.

The XPD remains comparable between the two cases, at approximately 21 dB for both configurations, indicating that the scattering plate does not significantly alter the polarization purity of the field, the polarization tilt angle at the QZ center decreases marginally from 3.33° to 0.7° with the plate introduced, which is attributed to partial cancellation of the E_z component due to the additional scattered field rather than a physical improvement in polarization alignment.

The summarized results are presented in Table 4.5 and Table 4.6 respectively with all metrics displayed.

Table 4.5: Case 2: Offset reflector with serrated edges at 4 GHz

Metric	**Horizontal**	**Vertical**
QZ Size (m)	1.5000	1.5000
Magnitude		
Mean (dB)	−0.1568	−0.1551
RMS (linear)	0.0409	0.0398
RMS (dB)	−27.7	−28
Pk-Pk (dB)	1.2498	1.2058
Std (dB)	0.3285	0.3188
XPD (dB)	21.5219	21.1895
Phase		
Mean (deg)	−1.5092	−1.5448
RMS (deg)	3.3710	3.3431
Pk-Pk (deg)	9.7081	9.7761
Std (deg)	3.0295	2.9797

Center tilt angle = 3.33°

Table 4.6: Case 6: Scattering plate introduced in chamber

Metric	**Horizontal**	**Vertical**
QZ Size (m)	1.5000	1.5000
Magnitude		
Mean (dB)	0.7120	0.7939
RMS (linear)	0.1176	0.1185
RMS (dB)	−18.59	−18.52
Pk-Pk (dB)	2.7067	1.7672
Std (dB)	0.6237	0.5323
XPD (dB)	21.3111	20.3878
Phase		
Mean (deg)	−1.7530	−3.0817
RMS (deg)	5.0872	5.8335
Pk-Pk (deg)	17.5051	17.9110
Std (deg)	4.7997	4.9781

Center tilt angle = 0.7°

5

Conclusion

A simplified electromagnetic chamber model has been implemented as a first step toward a future digital-twin framework. The model includes key CATR components, such as the horn feed aperture, an approximate reflector representation, and a scattering plate. The field evaluation is performed in the QZ using horizontal and vertical cut planes and sampled field evaluations for post-processing analysis, with all components positioned according to the simplified chamber geometry used in this study.

In addition, a PO solver was developed and verified against an already validated MoM solver. The primary reason for selecting PO for the reflector was that it provides sufficient accuracy while remaining computationally efficient for electrically large structures. The MoM solver was used to validate both the PO implementation and to model a small scattering plate, where higher accuracy and the inclusion of diffraction effects are more important. This combination provides a practical balance between computational cost and solution accuracy, which is important for future digital twin applications, where simulations must be sufficiently accurate while remaining computationally efficient to support near real-time analysis and decision-making.

Although differences between the PO and MoM solvers can be observed in the results, for example in Fig. 4.5, these discrepancies are expected due to the different approximations employed by the two methods. The largest deviations are observed near the edges of the reflector, where the limitations of the PO approximation become more significant. Furthermore, the discrepancies increase with increasing distance between the source and the plate, as illustrated in Table 4.2. This trend can be interpreted as a consequence of changes in the feed illumination across the reflector aperture, which in turn influences the relative importance of edge regions where the PO approximation is less accurate.

As discussed in the theory chapter, the PO solver neglects diffraction effects and assumes each triangle element to represent an infinitely large surface with no current continuity between adjacent elements. In contrast, the MoM approach allows currents to flow between discretized elements, thereby capturing both diffraction effects and electromagnetic coupling between neighboring elements.

The ripple observed in the results is therefore believed to originate from the limitations of the PO approximation. Since diffraction effects are not modeled, inaccu-

racies arise in regions where diffracted fields contribute significantly to the overall field distribution. This interpretation is supported by the observed reduction in ripple when the reflector area is increased. Increasing the reflector size or introducing serrated edges enlarges the effective reflecting area and reduces edge-related effects, which in turn decreases the ripple level. This behavior is evident in Fig. 4.12, where both modified reflector configurations exhibit reduced ripple compared to the non-serrated configuration.

The results from the test cases therefore indicate that, within the current PO-based model, no specific diffraction-related effect of the serrated edges can be resolved. Instead, the observed improvement is primarily attributed to changes in the effective reflecting surface representation. This represents a limitation of the model, which cannot assess the true diffraction-reduction effect of serrations.

The developed simulation model was able to reproduce some qualitative characteristics of QZ behavior observed in physical OTA chambers, particularly the presence and spatial variation of ripple effects associated with reflector geometry and edge interactions. The introduction of the plate into the model degrades the QZ field, resulting in increased ripple. The ripple behavior follows the physical nature of the plate placement, becoming increasingly rapid across the QZ as noted in Fig. 4.17. Both the amplitude and phase distributions are affected, qualitatively matching the expected physical behavior. Although the absolute quantitative accuracy of the model is limited by the PO approximation, the framework can be suitable for comparative evaluation of quiet-zone degradation caused by a scattering plate and reflector modifications.

The framework demonstrates that simplified EM models can support controlled comparative studies, but measurement validation is needed before it can guide chamber-design decisions quantitatively towards future DT-OTA analysis.

5.1 Social, Ethical, and Sustainability Considerations

From a societal and sustainability perspective, the simulation-based OTA chamber model has the potential to reduce the need for repeated physical measurements and extensive chamber testing. This may contribute to more efficient use of chamber facilities, reduced measurement time and lower resource consumption during antenna and OTA system evaluation. In industrial environments where OTA chambers are heavily scheduled and costly to operate, simulation analysis could therefore improve both development efficiency and resource utilization.

However, ethical and technical considerations must also be taken into account when using simplified simulation frameworks. The model developed in this thesis has primarily been validated qualitatively but the quantitative agreement with measured chamber data has not yet been fully established. Consequently, caution should be used when interpreting quantitative predictions.

5.2 Future Work

Future work should focus on improving the accuracy and realism of the OTA chamber model, as well as further validating it against chamber specifications and available datasheet information. In addition, the chamber behavior at higher frequencies should be investigated further, since this was only explored to a limited extent due to long computational times and the limitations of the current PO approximation in accurately modeling diffraction effects.

Once a sufficiently accurate model has been achieved, measured chamber data could be incorporated to enable more rigorous verification of the simulation framework and benchmarking of the simulated results against real measurement data. Some possible approaches for improving the current model are discussed below.

To verify that the observed discrepancies originate from diffraction effects neglected by the PO approximation, a more rigorous analysis could be performed using a MoM simulation, which inherently accounts for diffraction phenomena. However, for large structures, such simulations become highly demanding in terms of computational time and memory requirements, making them impractical within the scope of this work.

An alternative improvement would be to incorporate a Physical Theory of Diffraction (PTD). In such an approach, standard PO could be applied to the main reflector surface, while PTD contributions are used to model the serrated edges more accurately. This would likely improve the prediction of edge-related scattering and diffraction phenomena.

A more accurate serration model is also expected to improve the simulation results, since the observed artifacts are believed to originate at the reflector edges due to PO neglecting diffraction, where these approximations are causing the artifacts. The results further indicate that the introduction of serrations improves the QZ performance. However, in this thesis the serrations were approximated to follow the parabolic shape of the reflector, and their exact geometry was not modeled accurately. In reality, the serrations do not perfectly follow the parabolic contour and are not perfectly triangular, as assumed in the simulation model.

Although the implemented feed model follows the measured radiation pattern reasonably well within the reflector subtended angles, it does not exhibit the desired Gaussian tapering behavior over the full angular range. A feed model with a more accurate Gaussian-like taper across all angles would likely improve the overall field representation and reduce unwanted edge illumination effects, which may otherwise influence the accuracy of full-chamber simulations. Furthermore, leakage from the feed and into the QZ was neglected in the current model and should be investigated further, since such effects are present in the real OTA chamber and may contribute to the measured field behavior.

A quantitative validation of the model should be carried out by comparing simulated results with measured QZ scans using an identical feed configuration, reflector geometry and frequency.

Bibliography

[1] C. A. Balanis, *Antenna Theory: Analysis and Design*, 3rd ed. Hoboken, NJ, USA: Wiley, 2005. [Online]. Available: https://ia800501.us.archive.org/30/items/AntennaTheoryAnalysisAndDesign3rdEd/Antenna%20Theory%20Analysis%20and%20Design%203rd%20ed.pdf [Accessed: Jan. 26, 2026].

[2] O. Borries, P. Meincke, E. Jørgensen, H.-H. Viskum, F. Jensen, and C. H. Schmidt, "Design and Validation of Compact Antenna Test Ranges using Computational EM," TICRA and Airbus Defence & Space, Copenhagen, Denmark. [Online]. Available: https://www.ticra.com/wp-content/uploads/2018/03/A15-0136.pdf [Accessed: May 19, 2026].

[3] Wikipedia, "Digital twin," Wikimedia Foundation. [Online]. Available: https://en.wikipedia.org/wiki/Digital_twin [Accessed: May 19, 2026].

[4] Digital Twin Consortium, "The Definition of a Digital Twin," Digital Twin Consortium. [Online]. Available: https://www.digitaltwinconsortium.org/initiatives/the-definition-of-a-digital-twin/. [Accessed: May 19, 2026].

[5] M. Nikolova, "Lecture 8: Antenna Measurement," McMaster University. [Online]. Available: https://www.ece.mcmaster.ca/faculty/nikolova/antenna_dload/current_lectures/L08_Measure.pdf [Accessed: Jan. 14, 2026].

[6] P.-S. Kildal, *Foundations of Antennas: A Unified Approach for Line-of-Sight and Multipath*, Lund, Sweden: Studentlitteratur AB, 2000, p. 138.

[7] L. Ludwig, "My Thoughts on Ludwig's Polarization Definitions," [Online]. Available: https://zinka.wordpress.com/wp-content/uploads/2011/07/my-thoughts-on-ludwig-polarization-definitions-i1.pdf [Accessed: May 19, 2026].

[8] A. C. Ludwig, "The Definition of Cross Polarization," *IEEE Transactions on Antennas and Propagation*, vol. 21, no. 1, pp. 116–119, Jan. 1973. [Online]. Available: https://ieeexplore.ieee.org/document/1140406 [Accessed: May 19, 2026].

[9] C. A. Balanis, *Advanced Engineering Electromagnetics*, 2nd ed. Hoboken, NJ, USA: Wiley, 2012, p. 18. [Online]. Available: https://ndl.ethernet.edu.et/bitstream/123456789/88007/4/

Balanis-AdvancedEngineeringElectromagnetics-2012.pdf [Accessed: Feb. 02, 2026].

[10] "Lecture 4L – Electrostatic Boundary Conditions," EM Possible, Accessed May 5, 2026. [Online]. Available: https://empossible.net/academics/emp3302/ [Accessed: Feb. 05, 2026].

[11] M. Carlsson, "Method of Moments for Maxwell's Equations Based on Higher-Order Interpolatory Representation of Geometry and Currents," Master's thesis, Dept. of Signals and Systems, Chalmers Univ. of Technology, Gothenburg, Sweden, 2016. [Online]. Available: https://odr.chalmers.se/server/api/core/bitstreams/0d3ff7a2-4491-45eb-a283-54f2ea83aa29/content [Accessed: Feb. 02, 2026].

[12] Y. M. Wu and W. C. Chew, "The Modern High Frequency Methods for Solving Electromagnetic Scattering Problems," *Progress In Electromagnetics Research*, vol. 156, pp. 63–82, 2016.

[13] J. Volakis, A. Chatterjee, and L. C. Kempel, *Finite Element Method for Electromagnetics: Antennas, Microwave Circuits, and Scattering Applications*. Piscataway, NJ, USA: IEEE Press, 1998. [Online]. Available: https://api.pageplace.de/preview/DT0400.9780511911361_A23683441/preview-9780511911361_A23683441.pdf [Accessed: Feb. 04, 2026].

[14] L. Bondeson, T. Rylander, and P. Ingelström, *Computational Electromagnetics*. New York, NY, USA: Springer, 2005. [Online]. Available: https://www.lmn.pub.ro/~daniel/ElectromagneticModelingDoctoral/Books/Computational%20EM/Bondeson-%20Computational%20%20Electromagnetics.pdf [Accessed: Feb. 04, 2026].

[15] K. S. Yee, "Numerical Solution of Initial Boundary Value Problems Involving Maxwell's Equations in Isotropic Media," *IEEE Transactions on Antennas and Propagation*, vol. 14, no. 3, pp. 302–307, May 1966. [Online]. Available: https://ieeexplore.ieee.org/stamp/stamp.jsp?arnumber=10907162 [Accessed: Feb. 04, 2026].

[16] A. Taflove and S. C. Hagness, "Review of the Finite-Difference Time-Domain Method for Numerical Modeling of Electromagnetic Wave Interactions with Arbitrary Structures," *Wave Motion*, vol. 43, no. 4, pp. 305–343, 2006. [Online]. Available: https://ieeexplore.ieee.org/stamp/stamp.jsp?tp=&arnumber=4678420 [Accessed: Feb. 04, 2026].

[17] D. S. Weile and E. Michielssen, eds., *Frontiers in Computational Electromagnetics: ACES Symposium Proceedings*. Cham, Switzerland: Springer, 2022. [Online]. Available: https://link.springer.com/book/10.1007/978-3-031-01712-4. [Accessed: Mar. 26, 2026].

[18] Wikipedia, "Physical optics," Wikimedia Foundation. [Online]. Available: https://en.wikipedia.org/wiki/Physical_optics. [Accessed: Jan. 28, 2026].

[19] R. Paknys, *Applied Frequency-Domain Electromagnetics*. Hoboken, NJ, USA: Wiley, 2016. [Online]. Available: https://onlinelibrary.wiley.com/doi/book/10.1002/9781119127444. [Accessed: Feb. 02, 2026].

[20] S. M. Rao, D. R. Wilton, and A. W. Glisson, "Electromagnetic Scattering by Surfaces of Arbitrary Shape," *IEEE Transactions on Antennas and Propagation*, vol. 30, no. 3, pp. 409–418, May 1982. [Online]. Available: https://ieeexplore.ieee.org/document/1142818. [Accessed: Jan. 28, 2026].

[21] P.-S. Kildal, *Foundations of Antennas: A Unified Approach for Line-of-Sight and Multipath*. Lund, Sweden: Studentlitteratur AB, 2000, p. 141.

[22] Wikipedia, "Dipole antenna – Hertzian dipole," Wikimedia Foundation. [Online]. Available: https://en.wikipedia.org/wiki/Dipole_antenna#Hertzian_dipole. [Accessed: Apr. 07, 2026].

[23] R. Paknys, *Applied Frequency-Domain Electromagnetics*. Hoboken, NJ, USA: John Wiley & Sons, 2016, p. 9. [Accessed: Feb. 07, 2026]

[24] M. Maschen, "Felder um Dipol," Wikimedia Commons, Sep. 16, 2012. [Online]. Available: https://commons.wikimedia.org/wiki/File:Felder_um_Dipol.svg [Accessed: May 22, 2026].

A

Boundary Conditions For The Electric Field

Consider the infinitesimal closed contour shown in Fig. 2.3a. Applying Faraday's law in integral form gives

$$\begin{aligned} 0 &= \oint \mathbf{E} \cdot d\mathbf{l} \\ &= \int_a^b \mathbf{E} \cdot d\mathbf{l} + \int_b^0 \mathbf{E} \cdot d\mathbf{l} + \int_0^c \mathbf{E} \cdot d\mathbf{l} \\ &+ \int_c^d \mathbf{E} \cdot d\mathbf{l} + \int_d^0 \mathbf{E} \cdot d\mathbf{l} + \int_0^a \mathbf{E} \cdot d\mathbf{l} \\ &= E_{1,t}\Delta w - E_{1,n}\frac{\Delta h}{2} - E_{2,n}\frac{\Delta h}{2} \\ &- E_{2,t}\Delta w + E_{2,n}\frac{\Delta h}{2} + E_{1,n}\frac{\Delta h}{2}. \end{aligned} \tag{A.1}$$

The normal-field contributions cancel, leaving

$$0 = E_{1,t}\Delta w - E_{2,t}\Delta w \quad \Longrightarrow \quad E_{1,t} = E_{2,t}. \tag{A.2}$$

B

Vector And Scalar Potentials Identities

Consider a scalar field ϕ. Applying the gradient operator to ϕ produces a vector field that describes the spatial rate of change of the scalar field in each coordinate direction. In Cartesian coordinates, the gradient is given by

$$\nabla\phi = \partial_x\phi\,\hat{\mathbf{x}} + \partial_y\phi\,\hat{\mathbf{y}} + \partial_z\phi\,\hat{\mathbf{z}}. \tag{B.1}$$

Now consider a vector field $\mathbf{A}$. Taking the divergence of a vector field produces a scalar quantity describing the net outward flux density of the field:

$$\nabla \cdot \mathbf{A} = \partial_x A_x + \partial_y A_y + \partial_z A_z. \tag{B.2}$$

The curl operator instead produces another vector field describing the local rotational behaviour of the vector field:

$$\nabla \times \mathbf{A} = (\partial_y A_z - \partial_z A_y)\hat{\mathbf{x}} + (\partial_z A_x - \partial_x A_z)\hat{\mathbf{y}} + (\partial_x A_y - \partial_y A_x)\hat{\mathbf{z}}. \tag{B.3}$$

For compact notation, define

$$\partial_x \equiv \frac{\partial}{\partial x}, \tag{B.4}$$

and similarly for higher-order derivatives,

$$\partial_{xy} \equiv \frac{\partial^2}{\partial x \partial y}. \tag{B.5}$$

B.1 Curl of the Gradient

Consider the curl of the gradient of a scalar field:

$$\nabla \times (\nabla\phi) = (\partial_{yz}\phi - \partial_{zy}\phi)\hat{\mathbf{x}} + (\partial_{zx}\phi - \partial_{xz}\phi)\hat{\mathbf{y}} + (\partial_{xy}\phi - \partial_{yx}\phi)\hat{\mathbf{z}}. \tag{B.6}$$

If the scalar field ϕ is sufficiently smooth and continuously differentiable, the order of mixed partial derivatives may be exchanged according to Clairaut's theorem:

$$\partial_{ij}\phi = \partial_{ji}\phi. \tag{B.7}$$

Each term therefore cancels with its corresponding counterpart, giving the vector identity

$$\nabla \times (\nabla\phi) = 0. \tag{B.8}$$

In most practical electromagnetic applications, the fields are sufficiently smooth for this identity to hold.

B.2 Divergence of the Curl

Now consider the divergence of the curl of a vector field $\mathbf{A}$:

$$\begin{aligned}\nabla \cdot (\nabla \times \mathbf{A}) &= \partial_x(\partial_y A_z - \partial_z A_y) + \partial_y(\partial_z A_x - \partial_x A_z) + \partial_z(\partial_x A_y - \partial_y A_x) \\ &= \partial_{xy} A_z - \partial_{xz} A_y + \partial_{yz} A_x - \partial_{yx} A_z + \partial_{zx} A_y - \partial_{zy} A_x \\ &= (\partial_{yz} A_x - \partial_{zy} A_x) + (\partial_{zx} A_y - \partial_{xz} A_y) + (\partial_{xy} A_z - \partial_{yx} A_z).\end{aligned} \tag{B.9}$$

Using the equality of mixed partial derivatives,

$$\partial_{ij} A_k = \partial_{ji} A_k, \tag{B.10}$$

all terms cancel, resulting in the vector identity

$$\nabla \cdot (\nabla \times \mathbf{A}) = 0. \tag{B.11}$$

C

Characterization Of The Field In The Quiet Zone

This appendix contains the characterization of the QZ for the first, third, fourth and fifth cases described in Section 3.7.

Table C.1: Case 1: QZ Metrics for non-serrated edge Reflector at 4 GHz.

Metric	**Horizontal**	**Vertical**
QZ Size (m)	1.3636	1.3788
Magnitude (within QZ region)		
Mean (dB)	1.0971	1.1009
RMS (linear)	0.1813	0.1846
RMS (dB)	−14.83	−14.67
Pk-Pk (dB)	3.2356	3.4430
Std (dB)	0.9030	0.9360
XPD (dB)	21.2689	20.7634
Phase		
Mean (deg)	−6.1071	−6.1688
RMS (deg)	10.4323	10.5362
Pk-Pk (deg)	28.9341	29.3992
Std (deg)	8.5048	8.5883

Table C.2: Case 3: QZ Metrics with Serrated Edges Reflector Evenly Illuminating at 4 GHz.

Metric	**Horizontal**	**Vertical**
QZ Size (m)	1.5000	1.5000
Magnitude (within QZ region)		
Mean (dB)	−0.1671	−0.1639
RMS (linear)	0.0366	0.0348
RMS (dB)	−28.73	−29.16
Pk-Pk (dB)	1.0987	0.9468
Std (dB)	0.2805	0.2641
XPD (dB)	18.6669	17.9190
Phase		
Mean (deg)	−1.4712	−1.5104
RMS (deg)	3.3263	3.2981
Pk-Pk (deg)	9.6693	9.5653
Std (deg)	2.9983	2.9467

Table C.3: Case 4: QZ metrics for Larger reflector with serrated edges at 4 GHz.

Metric	**Horizontal**	**Vertical**
QZ Size (m)	1.4394	1.4242
Magnitude (within QZ region)		
Mean (dB)	−0.2088	−0.2014
RMS (linear)	0.0378	0.0353
RMS (dB)	−28.45	−29.00
Pk-Pk (dB)	1.2831	1.1951
Std (dB)	0.2685	0.2442
XPD (dB)	21.6835	21.5833
Phase		
Mean (deg)	0.7990	0.8292
RMS (deg)	1.1792	1.1630
Pk-Pk (deg)	3.8935	3.8172
Std (deg)	0.8719	0.8198

Table C.4: Case 5: QZ Metrics for 20 dBi feed illuminating a Non-Serrated Edge Reflector at 4 GHz.

Metric	**Horizontal**	**Vertical**
QZ Size (m)	0.2879	0.2727
Magnitude (within QZ region)		
Mean (dB)	−0.0401	−0.1263
RMS (linear)	0.0470	0.0443
RMS (dB)	−26.55	−27.07
Pk-Pk (dB)	1.3150	1.1905
Std (dB)	0.4254	0.3865
XPD (dB)	23.7332	24.3210
Phase		
Mean (deg)	1.3900	1.1794
RMS (deg)	1.9291	1.6585
Pk-Pk (deg)	3.8524	3.3453
Std (deg)	1.3724	1.1980

DEPARTMENT OF ELECTRICAL ENGINEERING
CHALMERS UNIVERSITY OF TECHNOLOGY
Gothenburg, Sweden
www.chalmers.se

CHALMERS
UNIVERSITY OF TECHNOLOGY